

Investigation on strong vertical permeability and micro-pore characteristics of Jinan red clay using X-ray micro-tomography

Hao Cai

Shanghai Jiaotong University: Shanghai Jiao Tong University

Qi Zhang (✉ zhangqi33@sjtu.edu.cn)

Shanghai Jiaotong University: Shanghai Jiao Tong University <https://orcid.org/0000-0002-6679-4566>

Guanlin Ye

Shanghai Jiaotong University: Shanghai Jiao Tong University

Linhai Lu

Beijing Jiaotong University

Chaojun Wu

Jinan rail transit Group Co., Ltd

Fang Ji

Jinan rail transit Group Co., Ltd

Research Article

Keywords: X-ray micro-tomography, Red clay, Soil permeability, Three-dimensional pore network, Seepage simulation

Posted Date: March 23rd, 2022

DOI: <https://doi.org/10.21203/rs.3.rs-1320153/v1>

License:   This work is licensed under a Creative Commons Attribution 4.0 International License.

[Read Full License](#)

Version of Record: A version of this preprint was published at Environmental Earth Sciences on February 25th, 2023. See the published version at <https://doi.org/10.1007/s12665-023-10810-9>.

Abstract

Due to the peculiarity of the spring domain strata in Jinan, the phenomenon of serious water seepage appears in the process of excavation. The macro permeability of soil is closely correlated with its microstructure. In this study, by using the X-ray micro-tomography (micro-CT) system and a self-designed soil seepage device, the internal pore structure of Jinan red clay and the water flow inside the sample under different seepage stages were observed. The microstructure of water phase and air phase in the sample was segmented by the watershed algorithm. Calculation and comparison of pore and throat size distributions at different seepage stages were conducted by establishing Pore Network Model (PNM). Meanwhile, the seepage experiment simulations were conducted based on the 3D pore structure of red clay. The results show that the preferentially flow of Jinan red clay is obvious due to the existence of the vertically developed macropore channel. The fine particles (mainly silt particles) are washed away during seepage, thereby expanding the pore channels. The maximum pore radius and pore connectivity have important influence on seepage characteristics of Jinan red clay, but the correlation between porosity is small.

1 Introduction

During the construction of Jinan rail transit, engineers have encountered difficulties in excavation dewatering. Even with the construction of waterproof curtain, the dewatering problem of the foundation pit was still not completely solved, which brings great risks to the construction. Fig. 1 shows the water seepage at the bottom of a foundation pit in Peijiaying Metro Station. The water seepage is very likely to occur at the bottom of the excavation, where many visible pore channels exist. It is thus speculated that the long-term upward seepage of groundwater leads to the existence of vertical seepage channels in the Jinan red clay stratum, and thus reveals a strong vertical permeability.

Soil seepage is affected by many factors, including soil particle size (Liu et al. 2021; Zhang et al. 2018) mineral composition (Yan et al. 2020), soil pore structure (Zeng et al. 2011), saturation (Zuo et al. 2020), dynamic viscosity of pore fluid (Nguyen et al. 2013) and hydromechanical conditions (Chang et al. 2013; Yang 2020; Zhang 2014). Numerous studies conducted before has focused on the seepage characteristics of clay (Boynton and Daniel 1985; Huang and Laften 1996; Miller and Low 1963). Rolfe et al. (1977) examined the changes in permeability and salt sieving which accompany the flow through clay media and attempted to relate the changes in permeability to the mechanical and physicochemical properties of the clay system. Liu et al. (2020) performed a series of seepage experiments on methane hydrate-bearing clayey sediments to investigate non-Darcy and Darcy flow characteristics of saturated clay.

Most of the mentioned studies on seepage characteristics of clay are from macroscopic field. In the past few decades, the mesoscopic tests, including scanning electronic microscopy and digital image processing methods (Tang et al. 2012; Ni et al. 2021; Wang et al. 2020), have been developed to study the grain-scale soil behavior. As a non-destructive 3D reconstruction technology, X-ray micro-tomography (micro-CT) has been widely used in geotechnical engineering in recent years (Chen et al. 2021; Lyu et al. 2021; Taylor et al. 2015). Desrues et al. (1996) successfully observed shear bands under triaxial

conditions of sand using medical X-ray CT and described the development of the localization qualitatively and quantitatively. Otani et al. (2006) investigated the three dimensional failure patterns in sand due to a laterally loaded pile using X-ray CT. Higo et al. (2011) investigated localized deformation in partially saturated sand using micro-CT and digital image correlation (DIC) technique. There are also many studies using micro-CT on the microscopic characteristics of clay (Kariem et al. 2018; Pineda et al. 2016). Mukunoki et al. (2014) carried out indirect tensile tests of compacted clay liner (CCL) material subjected to cracking to characterize its sensitivity using the industrial X-ray CT. Wang et al. (2017) reported a detailed study of structural change in clay due to freeze–thaw by using 3D X-ray CT. Naveed et al. (2013) combined soil physical measurements including soil-water retention, air permeability and micro-CT to study the soil-pore structural development and functional macro-pore networks along a clay gradient.

Pore structure, which provides space for water movement, has a significant influence on the seepage characteristics of soil. The strong vertical permeability of Jinan red clay is closely related to its micro-pore characteristics. Micro-CT is a useful method to obtain the micro-pore characteristics of soil such as pore size distribution and connectivity. Combining seepage experiment and micro-CT scanning system is the most effective means to understand the reason for the strong permeability of Jinan red clay layer. In this study, the seepage experiment combined with X-ray micro-tomography was designed to obtain the micro-pore structure of Jinan red clay and visualize the seepage path of water. The watershed algorithm was validated and used to segment the microstructure of Jinan red clay, including soil particles, pore water and pore air. Calculation and analysis of pore and throat size distributions were conducted by establishing Pore Network Model (PNM). Meanwhile, the seepage experiment simulations were conducted based on the 3D structure of Jinan red clay. Results of microscopic changes of Jinan red clay under different seepage stages and the absolute permeability of different regions of interest (ROI) were presented and discussed in detail.

2 Engineering Background And Geological Conditions

Jinan is a famous city in China also widely known as "Spring City". The Quaternary sedimentary layer is mainly composed of clay and silty clay in Jinan, but shows high vertical permeability. The hypsography of Jinan is southern high and northern low-lying. After atmospheric precipitation, surface water seeps into the ground and flows from south to north. Fig. 2 is the schematic diagram of the formation of Jinan spring group. The stratum in the northern part of Jinan consists of Yanshanian intrusive rock, which is hard and impermeable. The groundwater is blocked here, converging from horizontal movement to vertical upward movement. A large amount of groundwater passes through karst fissures and forms gushing springs.

The geological profile near the Peijiaying Metro Station is shown in Fig. 3. The soil layer of the site is unevenly distributed, and the thickness of the filling layer is about 0.5-4.3 m. Loess is locally distributed under the filling layer. The elevation from 25.92 m to -6.18 m is the Quaternary silty clay and clay layer, which includes the typical high permeability Jinan red clay layer. The elevation from -6.18m to -29.58m is mainly gravel and silty clay containing gravel. The underlying bedrock of the site consists of diorite and limestone.

The stratum between permeable stratum and limestone are mainly composed of high permeable gravel layer and completely weathered diorite layer, due to which the permeable stratum is directly recharged by the underlying limestone fissure confined water. The underlying Ordovician limestone layer contains abundant karst water, resulting in a high groundwater level, and the water inflow during the excavation of Peijiaying Metro Station is significantly greater than other areas. The vertical permeability of the red clay layer is obtained very high through the field test. The particularity of this layer of red clay is also a part of the reason for the excavation seepage. The soil samples were obtained from the typical permeable red clay stratum of Yanglanhe formation in Jinan. Undisturbed samples were obtained using thin-walled tube sampling with PVC pipes. These sharp-edged pipes can avoid disturbance on the sample as much as possible for laboratory testing. The physical properties and the mineral composition are determined by X-ray diffraction (XRD) and is listed in Table 1. It is known that the organic carbon content of Jinan red clay is much higher than that of general clay, indicating that there may be carbonized plant roots during the deposition process. Therefore, it can be inferred that the red clay layer in Jinan has formed many vertically developed pores under the action of long-term vertical seepage, and there exists macropore channels, resulting in the high permeability of these layers of soil.

Table 1 Physical properties and mineral composition of Jinan red clay

Physical properties					Mineral composition (%)			
Particle density (g/cm ³)	Initial void ratio	Natural water content (w _n /%)	Hydraulic conductivity (m/d)	Organic carbon content (%)	Quartz	Illite	Albite	Montmorillonite
1.99	0.701	25.40	1.22	12.18	42.4	40.2	16.8	0.6

In order to verify the conjecture, the seepage experiment of Jinan red clay was designed based on X-ray micro-tomography to obtain the micro-pore structure of Jinan red clay and observe seepage path of water in the soil sample.

3 Testing Procedure And Technology

3.1 Testing procedure

Three red clay samples from different parts of intact soil column are trimmed into a cylinder with diameter of 5 cm and height of 10 cm (Fig. 4) followed by scanning of three intact samples by micro-CT to obtain the pore characteristics of Jinan red clay at different depths. The first micro-CT scanning experiment for top sample (T1) has lower spatial resolution to get a wider scanning field. The middle (M1) and bottom (B1) samples were scanned with a higher spatial resolution to observe the internal pore morphology of red clay more distinctly, and the middle sample (M1) was adopted in the seepage experiment.

Fig. 5 shows the schematic figure and photo of seepage experiment for Jinan red clay. The seepage apparatus made of PMMA is designed as two parts, the main body and the base, which are connected with each other through screw threads. First, the sample is trimmed into a cylinder with diameter of 5 cm and height of 10 cm. Then the sample is put into the PMMA container with silicone grease on each side, and the main body and the base are screwed by threads. The prepared gypsum liquid is dropped into the gap between the sample and the side wall of the container to prevent water from flowing up from the gap. Finally, two sealing hoops are added at the bottom and top of the apparatus body to ensure that the container is sealed. A channel is set up in the base and connected with a plunger pump (GDS Instruments Co., UK) for external water supply to simulate the seepage of water from bottom to top in the soil. The seepage apparatus is fixed on the rotation stage between the X-ray source and the detector as shown in Fig. 6, which enables the seepage apparatus to be rotated by plus or minus 180° during scanning.

The whole seepage experiment based on micro-CT is divided into three stages: 1) intact sample (M1); 2) Intermediate stage of seepage experiment; 3) End stage of seepage experiment. The time of water flowing from the bottom to the top of the sample is determined by a large number of preliminary experiments, and the approximate time from the water flow to the middle of the scanning range is estimated. In this seepage experiment, with a water supply pressure of 10 kPa provided by a plunger pump (GDS Instruments Co., UK), the time of water supply of the intermediate stage and end stage is 6 minutes and 35 minutes respectively. The water injected into the sample is added with iohexol, a water-soluble X-ray contrast medium, to make it easier to distinguish water and air in soil.

The micro-CT apparatus used in this study is the Zeiss Xradia 520 Versa in Instrumental Analysis Center of Shanghai Jiao Tong University. The micro-CT system was operated at a voltage of 140 kV and a current of 71.6 and the X-ray power was 10 W during the scanning process. The partial CT scan with cylinder scanning field of a diameter of 2.5 cm and a height of 2.5 cm in the middle of the sample is used to avoid the boundary effects (Fig. 7). The specification of the X-ray CT system and the parameters used in this study are shown in Table 2. All parameters in the three stages of the seepage experiment are taken same during scanning to make the comparison more scientific.

Table 2. Specification of the X-ray CT system

X-ray source	Maximum voltage	160 kV
	Minimum voltage	30 kV
	Maximum current	1mA
	Maximum spatial resolution	700 nm
Image Intensifier	Size of detector	9 inch
	CCD pixel size	20482
CT image	Voxel size (um)	T1: 48.82 ×49.3
		M1: 25.02 ×24.6
		B1: 26.12 ×26.3
	Exposure time (s)	T1: 2
		M1: 3.5
		B1: 3.5
Scanning method	Partial scan	

3.2 X-ray micro-tomography and Image analysis

X-ray micro-tomography is a non-destructive technology which allows visualization and quantification of internal features of objects by creating images and 3D reconstruction. X-ray is converted to visible light, and then transformed to digital data by CCD camera. Using the data, the computed tomography provides the distribution of the CT values, which is linearly related to linear attenuation coefficient obtained by:

$$I = I_0 \exp(-\mu x) \quad (1)$$

where I is the attenuated X-ray intensity, I_0 is the incident X-ray intensity, and x is the length through the object. In addition, the relation between density of objects and CT value are linear. Thus, the relative changes in density can be discussed through the changes in the CT values obtained under the same scanning conditions.

Fig. 8 illustrates the image processing procedure on a horizontal slice of the sample. The 16-bit slices of CT images are first converted into 8-bit gray-scale images by software Image J followed by application of a 3D median filter to remove the random noise. Following this process, the filtered image is segmented by “Moments” automatic threshold method in Image J. After that, the raw CT image is converted into filtered binary image shown in Fig. 8(d).

3.3 Watershed segmentation

The microstructure of water and air phase can be segmented by watershed algorithm. Watershed segmentation can be understood by interpreting the intensity image as a landscape (Wählby et al. 2004). This method was originally proposed by Beucher and Lantuejoul (1979), which aims to identify separate rainfall catchment basins. By analyzing valley topography, the boundary and the local minima are identified, and the boundary between basins is referred to as the 'watershed' boundary. Water will start to fill the local minima until contact is made with another valley, as shown in Fig. 9. At every point where two catchment basins meet, a watershed is built, and the images are segmented by these watersheds.

When segmenting more than two phases, a transition between high and low intensity phases may introduce artifacts with unwanted intermediate "coating" phase. Correct threshold cannot be easily and accurately determined with edges blurred by noise and partial volume effect. Partial volume effect is caused by resolution limits in image acquisition, which blurs the transition between phases and features, i.e., voxels do not map single homogeneous physical volumes (Avizo Software 9 User's Guide). The watershed technique provides an effective solution for these issues.

In this study, a region-based watershed algorithm is used to extract the pore air and water in Jinan red clay. Firstly, "conservative" thresholds are defined for defining initial seed markers for air and water in soil to avoid capturing noise. A gradient magnitude image is then calculated using quick Canny method (Canny, 1986), which could provide the landscape image controlling the expansion of markers. The image gradient gives useful hints on actual boundaries. The boundaries fit the optimal location in the transition between phase intensities based on the seed markers and the gradient image.

3.4 Validation of the methods

3.4.1 Validation of watershed segmentation method

The watershed segmentation method has been used in many researches (Yu et al. 2020; Wang et al. 2019; Zhou and Xiao 2019). To verify the effectiveness and accuracy of watershed segmentation method, an experiment is firstly carried out based on micro-CT in this study.

The red clay sample was trimmed into a cube with the size of 3.8cm×3.8cm×4.2cm (length×width×height). A hole was drilled from the top surface of the sample, which filled with a PMMA (Polymethylmethacrylate) tube, The PMMA tube was filled with a certain height of water, as shown in Fig. 10. Then the sample was scanned by micro-CT to visualize the air, water and soil particles in red clay.

Fig. 11 shows the results of typical horizontal section of the sample. Water, PMMA tube and the air are depicted in different color due to different density. The boundaries between the water and the PMMA tube, PMMA tube and air are distinguishable. Therefore, the watershed segmentation method of segmenting water, soil and pores is applicable. Based on the seed markers and the gradient image, the watershed expansion of the seed markers towards boundary is completed, and the air phase and water phase in soil

are successfully segmented and extracted as shown in Fig. 12. The effectiveness of the watershed segmentation is validated.

3.4.2 Validation of automatic threshold method.

Otsu (1979) proposed mostly widely adopted automatic threshold method, which is also available as an automatic threshold option in ImageJ. The “Moments” method proposed by Tsai (1985) attempts to preserve the moments of the original image in the threshold results, which has been proven to be applicable by experimental results. Comparing the two threshold methods applied to red clay (Fig. 13), Otsu’s method is more conservative, where numerous small pores were not identified.

Mercury Intrusion Porosimetry (MIP) were carried out on the Jinan red clay sample. The porosity of the sample calculated by Otsu’s and Moments threshold methods were 20.78% and 37.7% respectively, whereas the porosity measured by MIP was 39.5%. Hence, the Moments threshold method was applied in this study.

4 Results And Discussion

4.1 Pore structure of intact Jinan red clay

A series of CT slices (around 1020 in total) of the samples at different depths (Fig. 4) were acquired from micro-CT scanning. Following the image processing procedure, the CT images were reconstructed and segmented in the image processing software, Avizo (FEI Co., USA). The pore structure of intact Jinan red clay sample at different depths are shown as Fig. 14. It should be noted that the sample T1 has a wider scanning field with lower spatial resolution, thus the pore structure looks smaller than that of the other two samples. It is noticed that the pore structure of Jinan red clay at different depths mainly developed vertically with good connectivity. There are vertical pore channels with large pore diameter in all three samples.

4.2 Comparison between different stages of seepage experiment with CT scanning

As mentioned above, the density of objects is linearly related to the CT value. In CT images, regions of higher density are indicated by lighter color such as white or light gray, while the lower density regions are denoted by dark color such as black. Fig. 15 shows the typical horizontal cross sections of the Jinan red clay sample. It is observed that the clay particles are light gray and the difference between pores filled with water and unfilled pores is more discernible because of the addition of iohexol.

Fig. 16 (a)-(c) shows the vertical slices of 3D reconstruction of the sample under three stages. It can be observed that there is a connected pore channel in the left side of the sample in Fig. 16 (a). With the

progress of water supply, the water flowed along the channel in the sample. The water flowed to the middle of the seepage channel in the intermediate stage of seepage experiment and completely passed through the seepage channel at the end stage of seepage experiment as shown in Fig. 16 (b, c). Meanwhile, the diameter variation of the seepage channel at different positions under three stages were measured (Fig. 17). Three points with different distances from the top of the seepage channel were selected, including 2500 μm , 5000 μm , and 7500 μm . The diameter of seepage channel was observed to increase with the progress of seepage experiment, especially in the initial stage of water supply. The result indicates that the seepage channel expands during the seepage experiment.

The watershed segmentation was applied to separate and extract air phase and water phase from the sample under different seepage stages. Subsequently, a volume rendering module was applied to observe the 3D structure of air and water phase in soil (Fig. 18). It can be concluded that when water flows through the clay, it will flow preferentially along the existing connected pore channels of clay from the comparison between three stages as shown in Fig. 16 and Fig. 18.

After the seepage experiment, the soil particles washed out by water were collected and scanned by Laser particle size analyser (LPSA). The comparison of grain size distribution is shown in Fig. 19. It is known that the intact Jinan red clay is mainly composed of 10% sand, 40% silt, and 50% clay. The soil particles washed out by water are mainly fine particles, including 80% silt particles and 20% clay particles, and there are basically no sand particles. The seepage experiments with different water supply pressures were conducted on the T1 and M1 sample to check the authenticity of the result. The pressures were increased from 20kPa to 40kPa with the same water supply time for 90 minutes. Fig. 20 shows the comparison of grain size distribution of two intact samples and washed-out particles. With most of the silt particles and a small portion of the clay particles washed out, similar type of result was obtained. This fact attributes that seepage causes the pore ions concentration to reduce with a loss of clay mineral bonding strength, resulting in the detachment of silt particles from aggregates. Most particles of the Jinan red clay washed out by water are silt particles, indicating the clay particles have higher cohesion compared with silt particles, which makes it harder to get detached from aggregates. With the increase of pressure, the change of the grain size distributions is not obvious, indicating the pore structure of the soil is not damaged under the current pressure range, and the washed-out particles mainly come from the pore walls. Hence it can be concluded that water flow preferentially along the existing connected pore channel of clay, during which the fine particles are washed away, thereby expanding the seepage channels.

4.3 Analysis of the micro-pore characteristics based on the establishment of Pore Network Model (PNM)

After the reconstruction of pore space, the Pore Network Model (PNM) was established (Fig. 21), with air phase for intact sample, air phase and water phase for samples at intermediate stage and end stage of seepage experiment. In the PNM, the algorithm divides the pore space into pore bodies and pore throats, which are represented by red spheres and gray sticks shown in Fig. 22 respectively. The true pore sizes

were represented by the radius of sphere r_n (named EqRadius in Avizo, calculated for spheres with the same volume as an irregularly shaped pore body). The throats were modelled as cylinders using the contact area between two pore bodies, the stick thickness is the EqRadius of true throats and the throat length is represented by the distance between the pore centres along the direction of the pores. By generating the PNM, important macroscopic transport properties, including capillary pressure, relative permeability and residual saturation can be computed (Sakellariou et al. 2004; Zhao et al. 2019). Calculation and analysis of pore and throat size distributions at different seepage stages are conducted in this study. From Fig. 21, it is clear to see that the pores in intact Jinan red clay are mainly developed vertically and most of them are connected, indicating the good permeability of Jinan red clay in vertical direction. It can also be verified from the SEM image of Jinan red clay (Fig. 23), the soil particles in the vertical section are arranged more closely with less pores compared with the horizontal section.

Fig. 24 shows the pore and throat size distributions of Jinan red clay sample under three different stages of the whole experiment. The results indicate Jinan red clay is mainly composed of small pores with pore EqRadius less than 100 μm . From the comparison of pore and throat size distribution in the three stages, we can illustrate that the number of pores and throats with large EqRadius is increasing with the progress of seepage experiment (Fig. 15 (a), (c)). In the stage 2 and stage 3, the pores with EqRadius larger than 200 μm increase by 11.5% and 18.9% in number, and the throats with EqRadius larger than 150 μm increase by 44.1% and 110.3% in number, respectively, which means the expansion of seepage channel. The distribution of throat length presented in Fig. 15 (b) shows that throats with length larger than 500 μm increase by 1.3% and 3.7% in number, respectively. The result indicates that the distribution of pore throat length changes slightly during seepage experiment. It can be attributed that the pore structure of the soil has not been damaged in the initial stage of seepage, nor does it cause excessive migration of clay particles. This result is consistent with the comparison of grain size distribution shown in Fig. 19 and Fig. 20.

It is worth noticing that the expansion of macropore in Jinan clay is contrary to the results of the decrease of macropore size of compacted granular mixtures (Alonso et al. 2011) and silty loess (Zuo et al. 2020). The aggregates in soil will expand and occupy the macropores when subjected to water infiltration, as the montmorillonite content is over 90% in Alonso's study. However, the Jinan red clay has low aggregates expanding potential, considering the low montmorillonite content (0.6%). In our study for Jinan red clay, the detached fine particles were washed away, making the seepage channels expand. In the study conducted by Zuo, the detached fine particles were also observed, but there was no further suffusion occurred so that the macropores were occupied by detached particles.

Fig. 25 shows the distribution of pore volume proportion and throat surface area proportion of the sample under three different stages of the whole experiment. The results show that the proportion of pore volume and throat surface area both increases for large pores (>550 μm) and throats (>450 μm). With the proportion of pore volume increases from 13.75% to 18.65%, the proportion of throat surface area increases from 8.21% to 19.44%. The increase of the proportion of large pores and throats results in the decrease of the proportion of small pores and throats. The results indicate that when water flows in the red

clay, the macropore channels have major influence on the seepage characteristics of red clay, while the influence of small pores can be ignored.

Seepage experiment with X-ray computed tomography shows that under the influence of long-term vertical seepage, the pores in the undisturbed Jinan red clay are mainly developed vertically and most of them are connected, resulting in the good permeability of Jinan red clay in vertical direction. Due to the particularity of Jinan spring area stratum, the permeable stratum is directly recharged by the underlying Ordovician limestone layer, which contains abundant karst water. Therefore, during the excavation in areas such as Peijiaying Metro Station, serious excavation seepage problems have occurred even if waterproof curtains are installed. In this case, in addition to setting up waterproof curtain, it is also necessary to set up enough pumping wells or deep-well drainage systems to solve the seepage problem of the excavation in Jinan red clay area.

4.4 Absolute permeability computation based on seepage experiment simulations

Absolute permeability, which appears in Darcy's law as a constant coefficient, is defined as the measure of the ability of a porous material to transmit a single-phase fluid. In this study, the seepage experiment simulations were conducted based on the 3D pore structure of red clay using Avizo-Xlab Hydro module, and the absolute permeability of different Regions of Interest (ROI) were calculated. The absolute permeability $K(m^2)$ of soil is calculated by the Eq. (2).

$$K = \frac{Q\mu L}{A\Delta P} \quad (2)$$

Where, $Q (m^3/s)$ denotes the volumetric flow rate that goes through the porous media; $\mu (Pa \cdot s)$ is the dynamic viscosity of the flowing fluid, set as $0.001 Pa \cdot s$, representing the viscosity coefficient of water at $20^\circ C$; $L (m)$ is the length of the calculated sample, set as $0.005m$; $A (m^2)$ denotes the area of flow cross-section, set as $0.000025 m^2$; ΔP is the pressure difference applied in the vertical direction of the sample, which is also set as $10 kPa$.

The hydraulic conductivity $k(m/s)$ in Darcy's law can be converted from the value of absolute permeability K according to Eq. (3).

$$k = \frac{K\gamma_w}{\mu} \quad (3)$$

Where, k denotes the hydraulic conductivity; γ_w is the weight of the fluid, which refers to water ($9.8kg/m^3$) in this study. The micro-scale flow is solved based on the Navier-Stokes equation. To make the calculation

easier, a simplified Stokes' equation was used for the incompressible and Newtonian fluid in a steady and laminar flow manner (Eq. 4).

$$\begin{cases} \vec{\nabla} \cdot \vec{V} = 0 \\ \mu \nabla^2 \vec{V} - \vec{\nabla} P = 0 \end{cases} \quad (4)$$

Where, $\vec{\nabla}$ is the divergence operator; $\vec{\nabla}$ is the gradient operator; \vec{V} is the velocity of the fluid; ∇^2 is the Laplacian operator; P is the pressure of the fluid in the fluid phase of the material.

Three different ROI with same size ($5000 \times 5000 \times 5000 \mu\text{m}^3$) were extracted from the 3D pore structure of each intact Jinan red clay sample as shown in Fig. 26, where PF region represents the region with obvious preferential flow, and NPF region represents the area where there is no obvious preferential flow.

The seepage simulation results of streamlines for different ROI of three intact samples were demonstrated in Fig. 27. It can be observed that the number and distribution density of streamlines in the PF regions are greater than the other two NPF regions for three samples. And the seepage flow paths through the ROI box of the PF region are also more complete, with greater flow velocity. For NPF regions, the vast majority of the seepage streamlines are cut off halfway, especially for the NPF regions of T1 sample, the streamlines are almost invisible, indicating that there is almost no seepage in this area.

The results of absolute permeability K (μm^2) and the corresponding hydraulic conductivity k ($\times 10^{-6} \text{ m/s}$) were presented in Table 3. The results calculated by seepage simulations show that the value of absolute permeability, as well as hydraulic conductivity of PF region is two orders of magnitude higher than that of NPF region. It can be noted that the calculated value of hydraulic conductivity is lower than that obtained from field pumping test ($1.22 \text{ m/d} \approx 1.4 \times 10^{-5} \text{ m/s}$), even for PF regions. This can be attributed to the fact that the preferential flow phenomenon is more obvious in the actual stratum, and the size of the ROI is very small for the seepage simulation. Hence, some connected pores are cut off in DOI, making it impossible to have a positive impact on permeability. The hydraulic conductivity obtained from field pumping test is closer to that of PF region from seepage simulation, indicating the seepage characteristics of Jinan red clay are mainly dominated by the preferential flow region.

Table 3. The calculated results of seepage experiment simulation

Sample	ROI	Maximum pore EqRadius (μm)	Pore volume content($\phi/\%$)	Pore connectivity ($\beta/\%$)	Absolute permeability (μm^2)	Hydraulic conductivity ($\times 10^{-6}$ m/s)
T1	PF	1321	14.6	46.8	289.11	2.83
	NPF-1	32	10.8	1.2	0.16	0.0016
	NPF-2	40	12.3	2.7	0.17	0.0017
M1	PF	1061	13.3	38.7	146.01	1.43
	NPF-1	245	13.8	9.8	5.73	0.06
	NPF-2	368	12.7	13.2	9.30	0.09
B1	PF	1645	15.9	59.8	589.11	5.77
	NPF-1	434	10.6	17.5	11.58	0.11
	NPF-2	458	10.8	16.8	11.84	0.11

The maximum pore EqRadius, pore volume content, and pore connectivity of each ROI were also listed, where the pore volume content is the ratio of pore volume to the volume of ROI, the pore connectivity is the ratio of connected pore volume to the total pore volume. It can be known that the pore volume content of different ROI is similar, indicating the pore volume content has little influence on the soil permeability. The high hydraulic conductivity in the PF region is due to existence of large pores with good connectivity. Fig. 27 shows the relation between absolute permeability and different pore parameters. It is found that the absolute permeability increases with the maximum pore EqRadius and pore connectivity. The seepage characteristics for Jinan red clay is more complicated, which is less related to porosity, but closely related to the pore morphology, connectivity, and other factors. The seepage simulation results show that the maximum pore EqRadius and pore connectivity have important influence on seepage characteristics, which is consistent with the conclusion obtained from seepage experiment.

5 Conclusions

This paper proposes a method to identify the water flow and analyse changes of the micro-pore characteristics of clay under different seepage stages based on X-ray micro-tomography system. The 3D pore space of the sample under different seepage stages was quantitatively identified and characterized by some geometrical parameters based on PNM, such as pore size distribution, throat size distribution. The seepage experiment simulations were conducted and the pore parameters affecting the soil permeability were analysed. The main conclusions obtained in this study are as follows:

1. The unique pore structure and soil properties lead to the strong vertical permeability of Jinan red clay. The pore structure of Jinan red clay is mainly vertically developed with macropore channel existing, which can be attributed to the long-term vertical seepage and the decaying roots during sedimentation.
2. The seepage experiment of red clay based on micro-CT scanning was designed. The results show that water flows preferentially along the existing connected pore channels of clay, during which the fine particles (including 80% silt and 20% clay) are washed out, so that the seepage channels expand.
3. The equivalent Pore Network Model (PNM) representing pore structure of Jinan red clay was established, and the micro-pore parameters were quantified. The PNM results show that Jinan red clay is mainly composed of small pores with pore EqRadius less than 100 μm . In the process of seepage experiment, the number and the proportion of large pores ($>550 \mu\text{m}$) and large throats ($>450 \mu\text{m}$) tend to increase, indicating the seepage channels expand and the macropore channel has major influence on the seepage characteristics of red clay. The pore throat length is almost unchanged, implying the pore structure of the soil has not been damaged under current conditions.
4. The seepage experiment simulations were conducted based on the 3D pore structure of Jinan clay, and the absolute permeability of different ROI were calculated. The results show that the value of absolute permeability of PF region is two orders of magnitude higher than that of NPF region. The maximum pore EqRadius and pore connectivity have important influence on seepage characteristics of Jinan red clay, but the correlation between porosity is small.

Declarations

Acknowledgments

The financial support from the Shanghai Sailing Program (Grant No. 20YF1418500), National Natural Science Foundation of China (NSFC Grant No. 42072317), and Natural Science Foundation of Shandong Province (Grant No. ZR2020ME258) are gratefully acknowledged.

Statements and Declarations

We declare that we have no conflicts of interest to this work. We declare that we do not have any commercial or associative interest that represents a conflict of interest in connection with the work submitted.

References

1. Alonso EE, Romero E, Hoffmann C (2011) Hydromechanical behaviour of compacted granular expansive mixtures: Experimental and constitutive study. *Geotechnique*. 61, 329–344.
<https://doi.org/10.1680/geot.2011.61.4.329>
2. Beucher S, Lantuejoul C (1979) Use of watersheds in contour detection. In: Proc. Int. Workshop Image Process. CCETT, Rennes, France.

3. Boynton SS, Daniel DE (1985) Hydraulic conductivity tests on compacted clay. *J. Geotech. Eng.* 111(4), 465–478. [https://doi.org/10.1061/\(ASCE\)0733-9410\(1985\)111:4\(465\)](https://doi.org/10.1061/(ASCE)0733-9410(1985)111:4(465))
4. Canny J (1986). A computational approach to edge detection. *IEEE Trans. Pattern Anal. Mach. Intell.* PAMI-8, 679–698. <https://doi.org/10.1109/TPAMI.1986.4767851>
5. Chang DS, Zhang LM (2013) Critical hydraulic gradients of internal erosion under complex stress states. *J. Geotech. Geoenviron. Eng.* 139(9), 1454–1467. [https://doi.org/10.1061/\(ASCE\)GT.1943-5606.0000871](https://doi.org/10.1061/(ASCE)GT.1943-5606.0000871)
6. Chang DS, Zhang LM (2014) A stress-controlled erosion apparatus for studying internal erosion in soils. *Geotech Test J.* 34(6), 579-589. <https://doi.org/10.1520/GTJ103889>
7. Chen Y, Ma G, Zhou W, Wei D, Zhao Q, Zou Y (2021) An enhanced tool for probing the microscopic behavior of granular materials based on X-ray micro-CT and FDEM. *Comput. Geotech.* 132, 103974. <https://doi.org/10.1016/j.compgeo.2020.103974>
8. Desrues J, Chambon R, Mokni M, Mazerolle F (1996) Void ratio evolution inside shear bands in triaxial sand specimens studied by computed tomography. *Geotechnique.* 46, 529–546. <https://doi.org/10.1680/geot.1996.46.3.529>
9. Higo Y, Oka F, Kimoto S, Sanagawa T, Matsushima Y (2011) Study of strain localization and microstructural changes in partially saturated sand during triaxial tests using microfocus X-ray CT. *Soils Found.* 51, 95–111. <https://doi.org/10.3208/sandf.51.95>
10. Huang C, Laften JM (1996) Seepage and soil erosion for a clay loam soil. *Soil Sci. Soc. Am. J.* 60, 408–416. <https://doi.org/10.2136/sssaj1996.03615995006000020011x>
11. Kariem H, Hellmich C, Kiefer T, Jäger A, Füssl J (2018) Micro-CT-based identification of double porosity in fired clay ceramics. *J. Mater. Sci.* 53, 9411–9428. <https://doi.org/10.1007/s10853-018-2281-9>
12. Liu Y, Yin ZY, Wang L, Hong Y (2021) A coupled CFD – DEM investigation of internal erosion considering suspension flow. *Can. Geotech. J.* 58(9), 1411–1425.
13. Lyu Q, Wu H, Li X (2021) A 3D model reflecting the dynamic generating process of pore networks for geological porous media. *Comput. Geotech.* 140, 104444. <https://doi.org/10.1016/j.compgeo.2021.104444>
14. Miller RJ, Low PF (1963) Threshold gradient for water flow in clay systems. *Soil Sci. Soc. Am. J.* 27, 605–609.
15. Mukunoki T, Nakano T, Otani J, Gourc JP (2014) Study of cracking process of clay cap barrier in landfill using X-ray CT. *Appl. Clay Sci.* 101, 558–566. <https://doi.org/10.1016/j.clay.2014.09.019>
16. Naveed M, Moldrup P, Arthur E, Wildenschild D, Eden M, Lamandé M, Vogel HJ, Jonge LW (2013) Revealing soil structure and functional macroporosity along a clay gradient using x-ray computed tomography. *Soil Sci. Soc. Am. J.* 77(2), 403–411. <https://doi.org/10.2136/sssaj2012.0134>
17. Nguyen XP, Cui YJ, Tang AM, Deng YF, Li XL, Wouters L (2013) Effects of pore water chemical composition on the hydro-mechanical behavior of natural stiff clays. *Eng. Geol.* 166, 52–64. <https://doi.org/10.1016/j.enggeo.2013.08.009>

18. Ni X, Ye B, Zhang F, Feng X (2021) Influence of specimen preparation on the liquefaction behaviors of sand and its mesoscopic explanation. *J. Geotech. Geoenvironmental Eng.* 147, 04020161. [https://doi.org/10.1061/\(asce\)gt.1943-5606.0002456](https://doi.org/10.1061/(asce)gt.1943-5606.0002456)
19. Otani J, Pham KD, Sano J (2006) Investigation of failure patterns in sand due to laterally loaded pile using X-ray CT. *Soils Found.* 46, 529–535. <https://doi.org/10.3208/sandf.46.529>
20. Otsu N (1979) A threshold selection method from gray-level histograms. *IEEE Trans. Syst. Man Cybern.* 9(1), 62–66.
21. Pineda JA, Liu XF, Sloan SW, (2016) Effects of tube sampling in soft clay: A microstructural insight. *Geotechnique.* 66, 969–983. <https://doi.org/10.1680/jgeot.15.P217>
22. Rolfe PF, Aylmore LAG (1977) Water and salt flow through compacted clays: I. permeability of compacted illite and montmorillonite. *Soil Sci. Soc. Am. J.* 41(3), 489–495. <https://doi.org/10.2136/sssaj1977.03615995004100030011x>
23. Sakellariou A, Sawkins TJ, Senden TJ, Limaye A (2004) X-ray tomography for mesoscale physics applications. *Phys. A Stat. Mech. its Appl.* 339(1-2), 152–158. <https://doi.org/10.1016/j.physa.2004.03.055>
24. Tang YQ, Zhou J, Hong J, Yang P, Wang JX (2012) Quantitative analysis of the microstructure of Shanghai muddy clay before and after freezing. *Bull. Eng. Geol. Environ.* 71, 309–316. <https://doi.org/10.1007/s10064-011-0380-9>
25. Taylor HF, O’Sullivan, C, Sim WW (2015) A new method to identify void constrictions in micro-CT images of sand. *Comput. Geotech.* 69, 279–290. <https://doi.org/10.1016/j.compgeo.2015.05.012>
26. Tsai WH (1985) Moment-preserving thresholding: a new approach. *Comput. Vision, Graph. Image Process.* 29(3), 377–393. [https://doi.org/10.1016/0734-189x\(85\)90133-1](https://doi.org/10.1016/0734-189x(85)90133-1)
27. Wählby C, Sintorn IM, Erlandsson F, Borgefors G, Bengtsson E (2004) Combining intensity, edge and shape information for 2D and 3D segmentation of cell nuclei in tissue sections. *J. Microsc.* 215, 67–76. <https://doi.org/10.1111/j.0022-2720.2004.01338.x>
28. Wang K, Zhang S, DelgadoTéllez R, Wei F (2019) A new slope unit extraction method for regional landslide analysis based on morphological image analysis. *Bull. Eng. Geol. Environ.* 78, 4139–4151. <https://doi.org/10.1007/s10064-018-1389-0>
29. Wang P, Guo X, Sang Y, Shao L, Yin Z, Wang Y (2020) Measurement of local and volumetric deformation in geotechnical triaxial testing using 3D-digital image correlation and a subpixel edge detection algorithm. *Acta Geotech.* 15, 2891–2904. <https://doi.org/10.1007/s11440-020-00975-z>
30. Wang S, Yang ZJ, Yang P (2017) Structural change and volumetric shrinkage of clay due to freeze-thaw by 3D X-ray computed tomography. *Cold Reg. Sci. Technol.* 138, 108–116. <https://doi.org/10.1016/j.coldregions.2017.03.007>
31. Yan S, Wang G, Wang Q, Li H, Wang W (2020) Characteristics of seepage of microemulsions in coal. *J. Mol. Liq.* 304, 112742. <https://doi.org/10.1016/j.molliq.2020.112742>

32. Yang J, Yin ZY, Laouafa F, Hicher PY (2020) Three-dimensional hydromechanical modeling of internal erosion in dike-on-foundation. *Int. J. Numerical and Analytical Methods in Geomechanics*. 44(8), 1200–1218. <https://doi.org/10.1002/nag.3057>
33. Yu B, Fan W, Fan JH, Dijkstra TA, Wei YN, Wei TT (2020) X-ray micro-computed tomography (μ -CT) for 3D characterization of particle kinematics representing water-induced loess micro-fabric collapse. *Eng. Geol.* 279. 105895. <https://doi.org/10.1016/j.enggeo.2020.105895>
34. Zeng LL, Hong ZS, Cai YQ, Han J (2011) Change of hydraulic conductivity during compression of undisturbed and remolded clays. *Appl. Clay Sci.* 51, 86–93. <https://doi.org/10.1016/j.clay.2010.11.005>
35. Zhang Z, Sui W, Wang K, Tang G, Li X (2018) Changes in particle size composition under seepage conditions of reclaimed soil in Xinjiang, China. *Processes*. 6(10), 201. <https://doi.org/10.3390/pr6100201>
36. Zhao Y, Zhu G, Liu S, Wang Y, Zhang C (2019) Effects of pore structure on stress-dependent fluid flow in synthetic porous rocks using microfocus x-ray computed tomography. *Transp. Porous Media*. 128, 653–675. <https://doi.org/10.1007/s11242-019-01264-4>
37. Zhou, XP, Xiao N (2019) Analysis of fracture properties of three-dimensional reconstructed rock model using hierarchical-fractal annealing algorithm. *Eng. Geol.* 256, 39–56. <https://doi.org/10.1016/j.enggeo.2019.04.017>
38. Zuo L, Xu L, Baudet BA, Gao C, Huang C (2020) The structure degradation of a silty loess induced by long-term water seepage. *Eng. Geol.* 272, 105634. <https://doi.org/10.1016/j.enggeo.2020.105634>

Figures



(a)

(b)

Figure 1

Photos of permeable foundation pit in Jinan: (a) Water seepage in excavation (b) Water seepage details

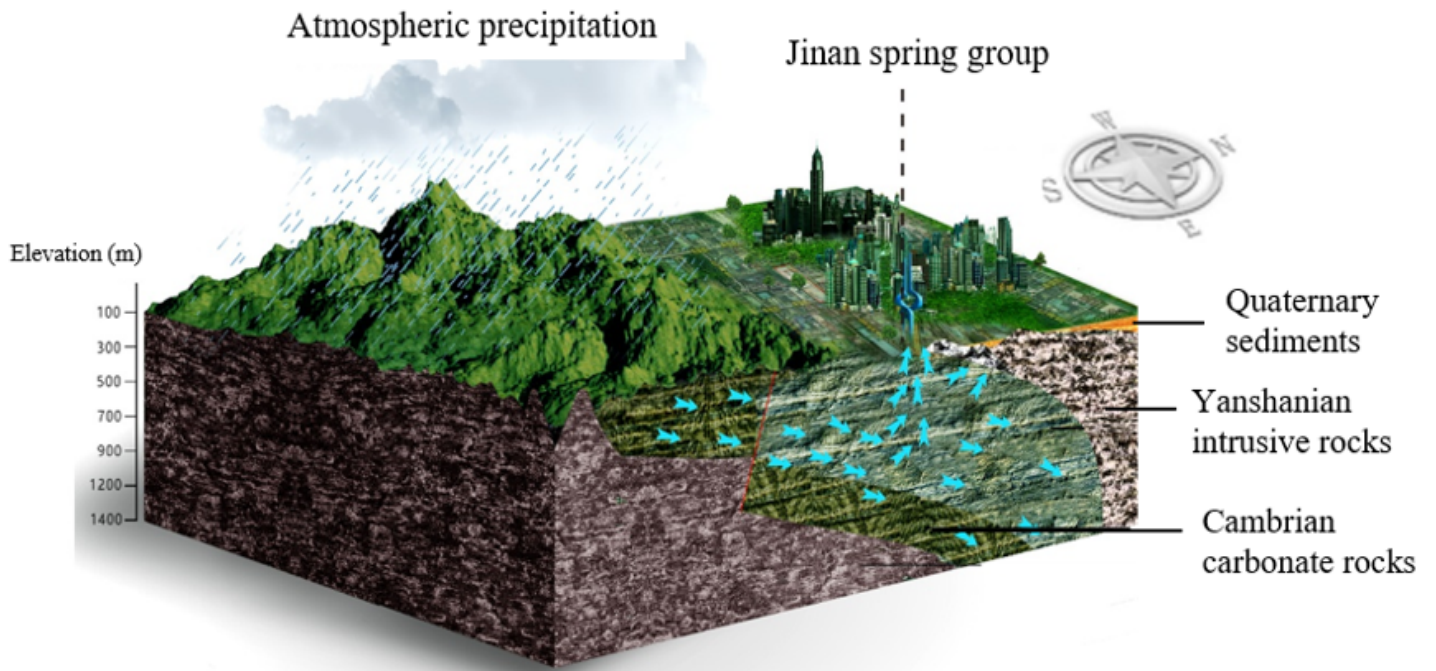


Figure 2

The formation of Jinan spring group

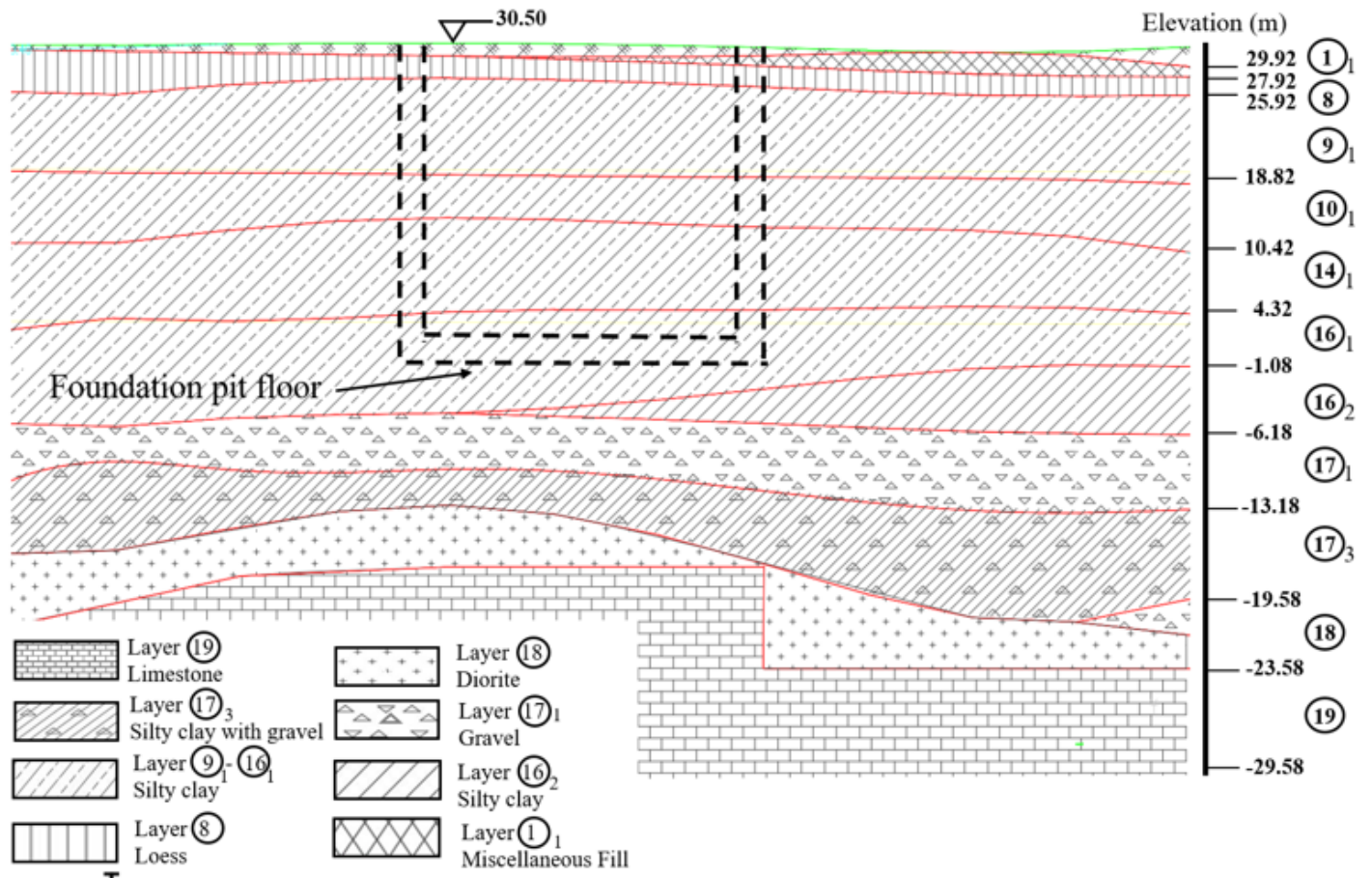


Figure 3

Stratum map of permeable foundation pit in Jinan

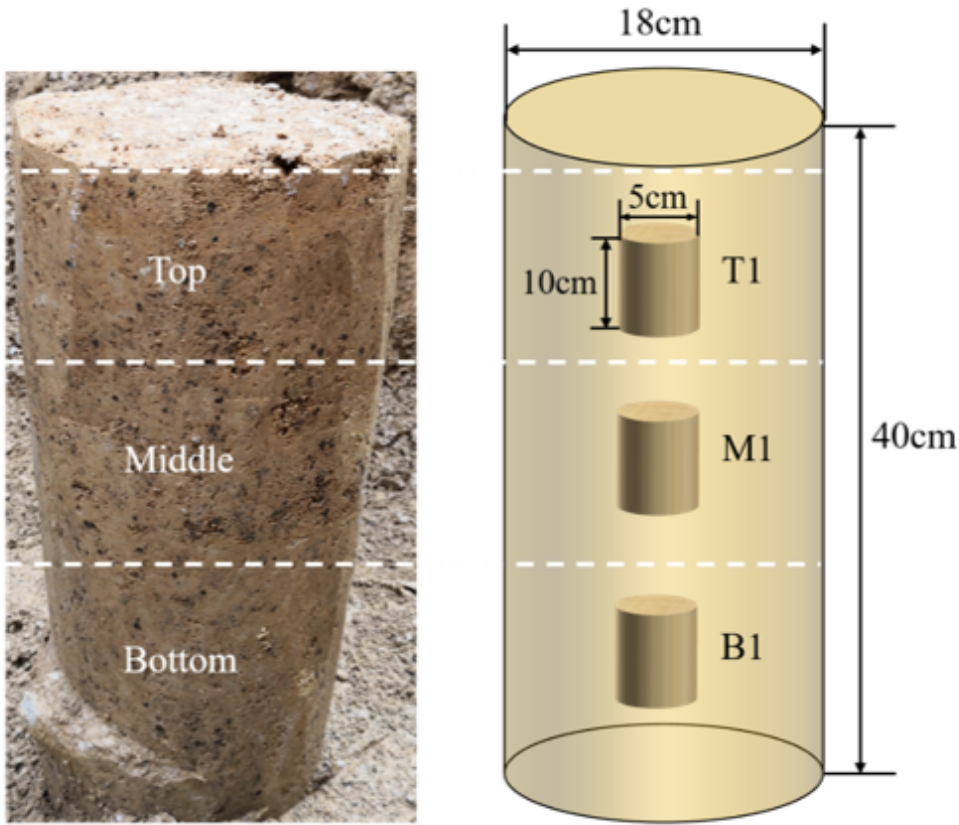


Figure 4

Intact Jinan red clay column and the sample positions

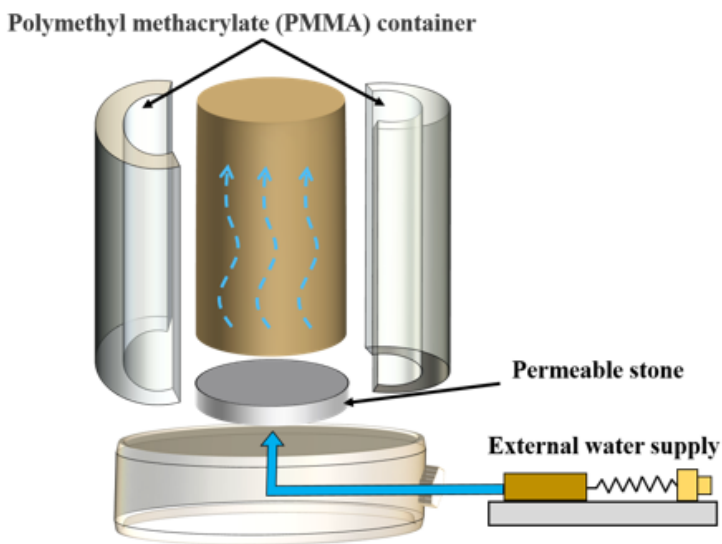


Figure 5

Schematic figure and photo of seepage experiment: (a) Schematic figure (b) Photo

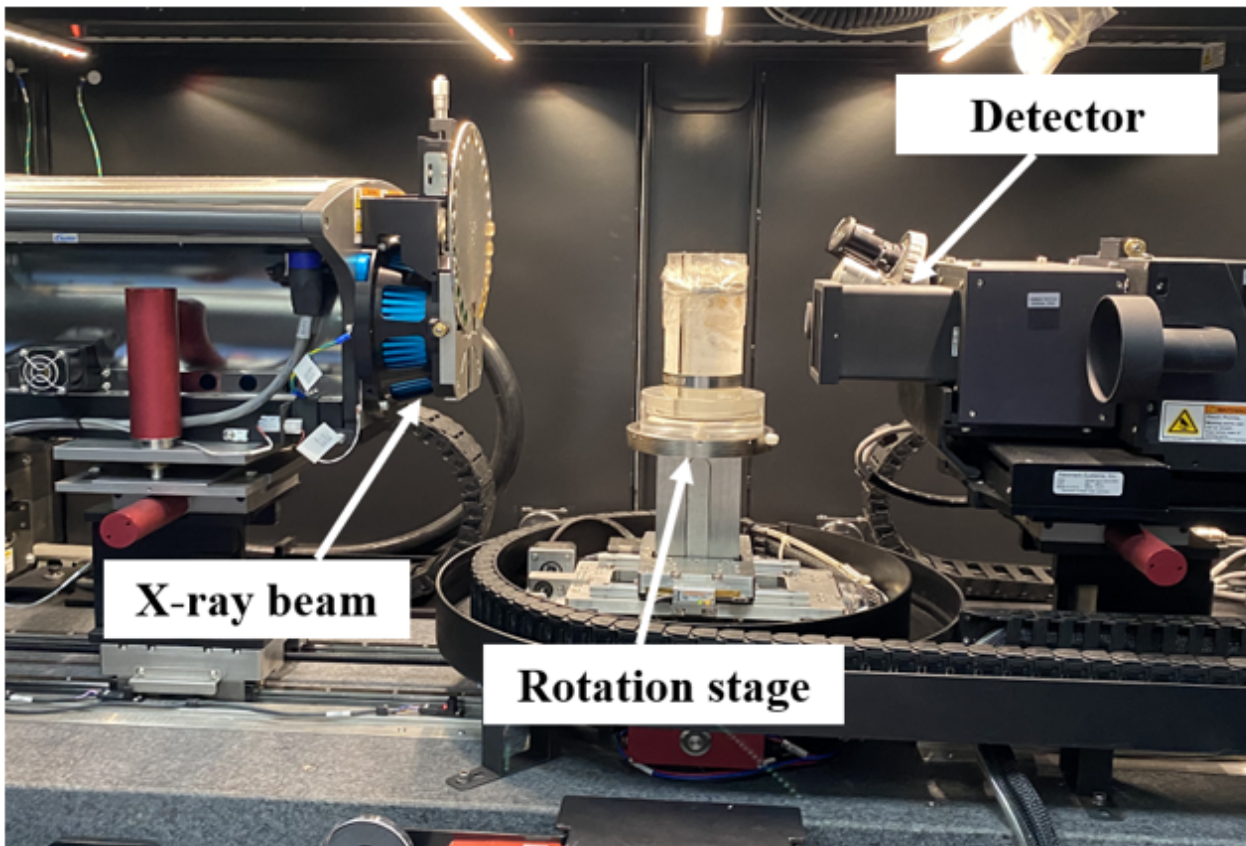


Figure 6

X-ray micro-tomography setup and seepage apparatus

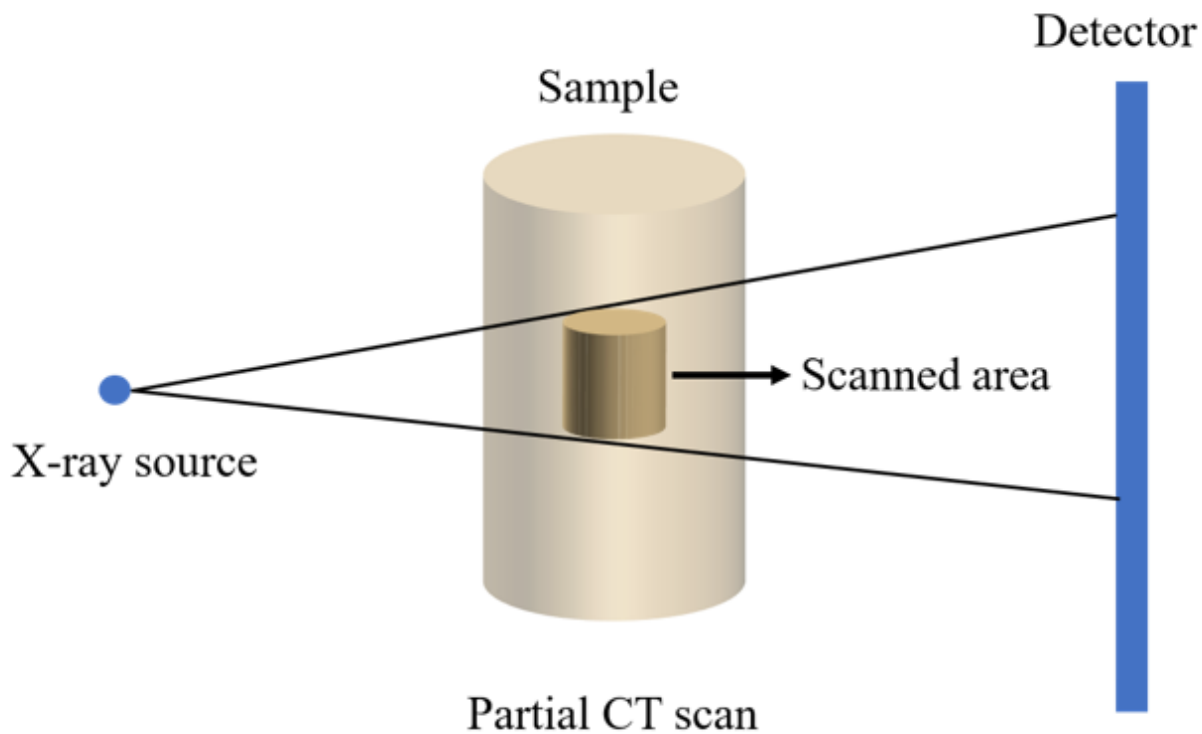


Figure 7

Schematic figure of partial CT scan

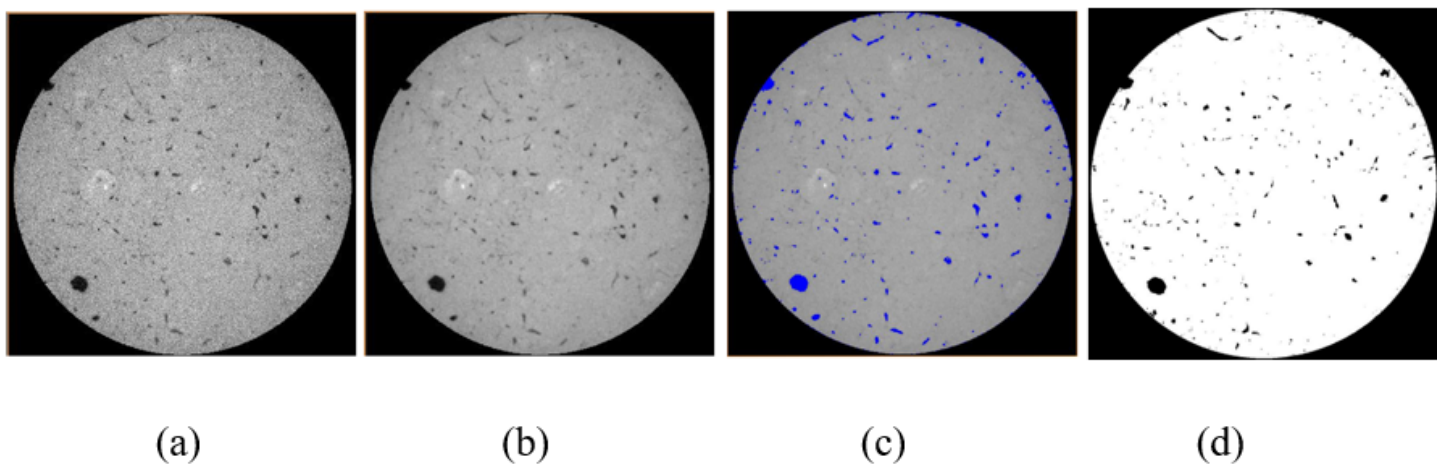


Figure 8

Illustration of image processing procedure on a horizontal slice of the sample before seepage experiment. (a) raw picture (b) after applying 3D median filter (c) during threshold segmentation (d) final segmented image

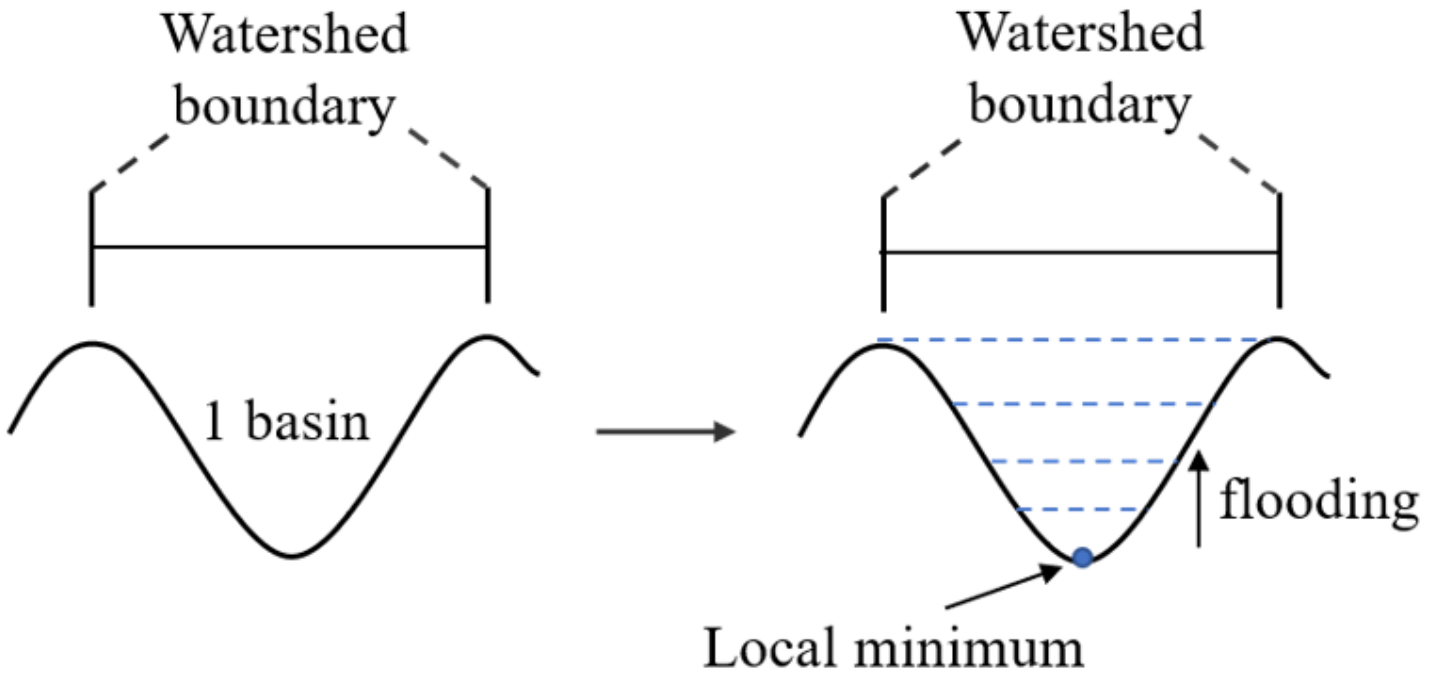


Figure 9

Conceptual example of watershed segmentation

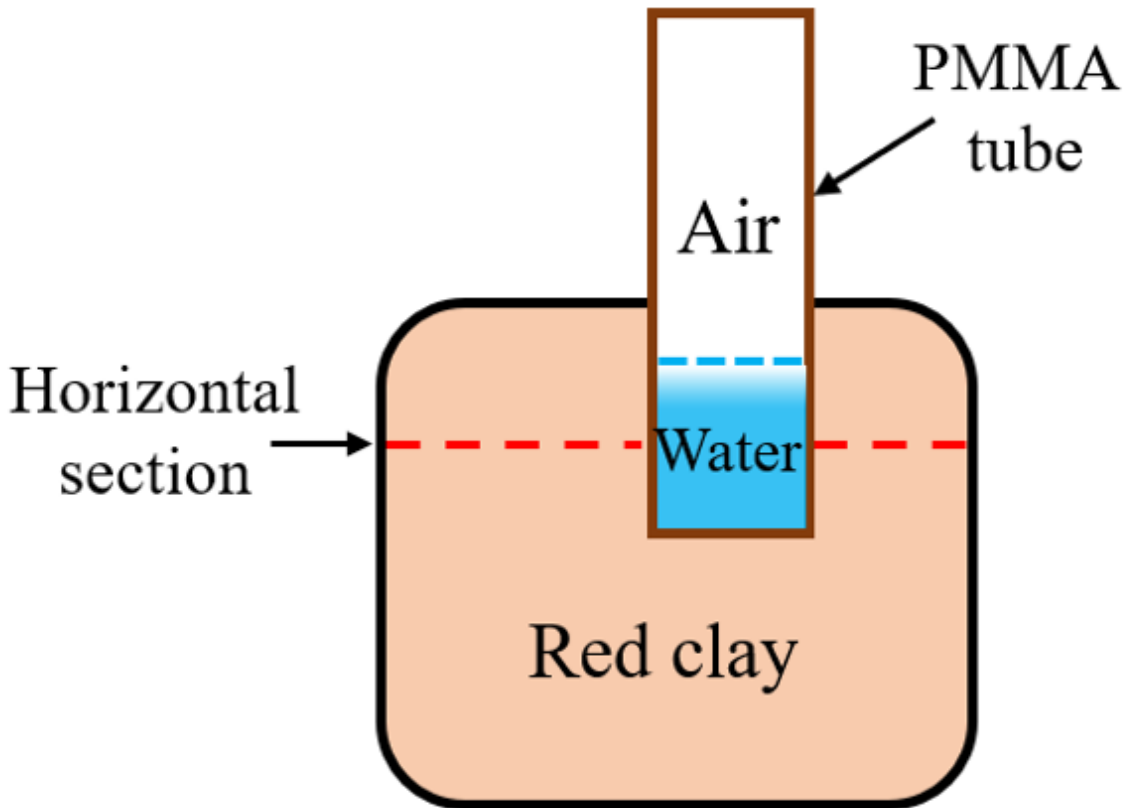


Figure 10

The picture and schematic diagram of the sample. (a) Picture (b) Schematic diagram

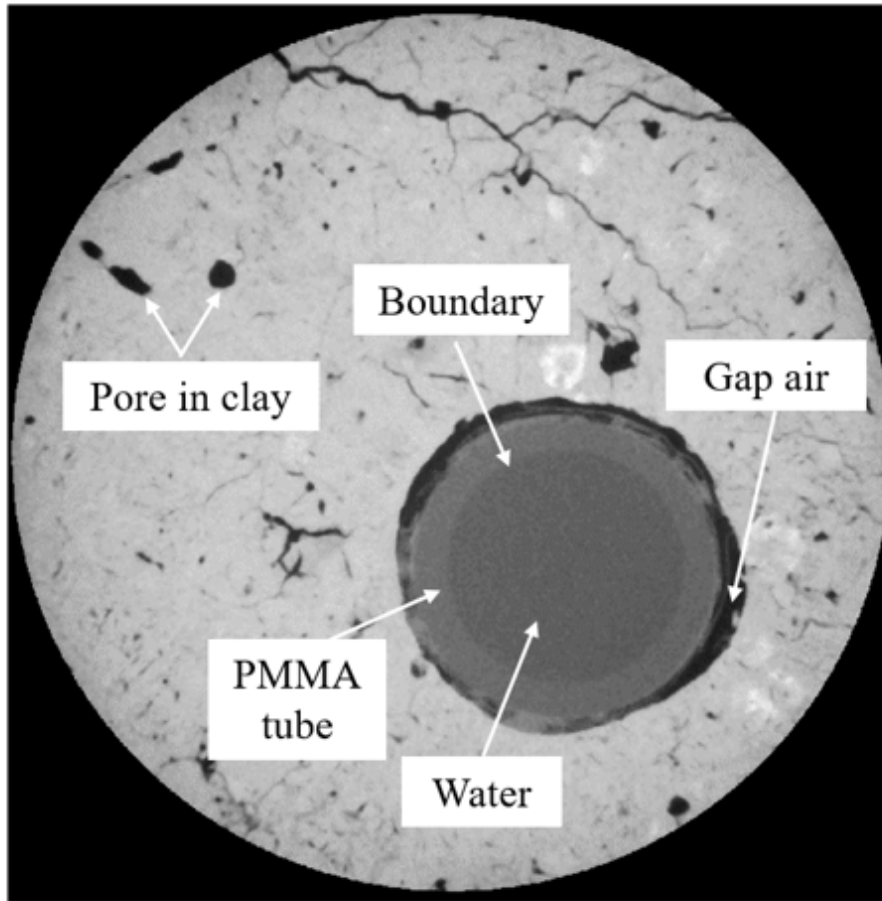


Figure 11

Typical horizontal cross section of the sample

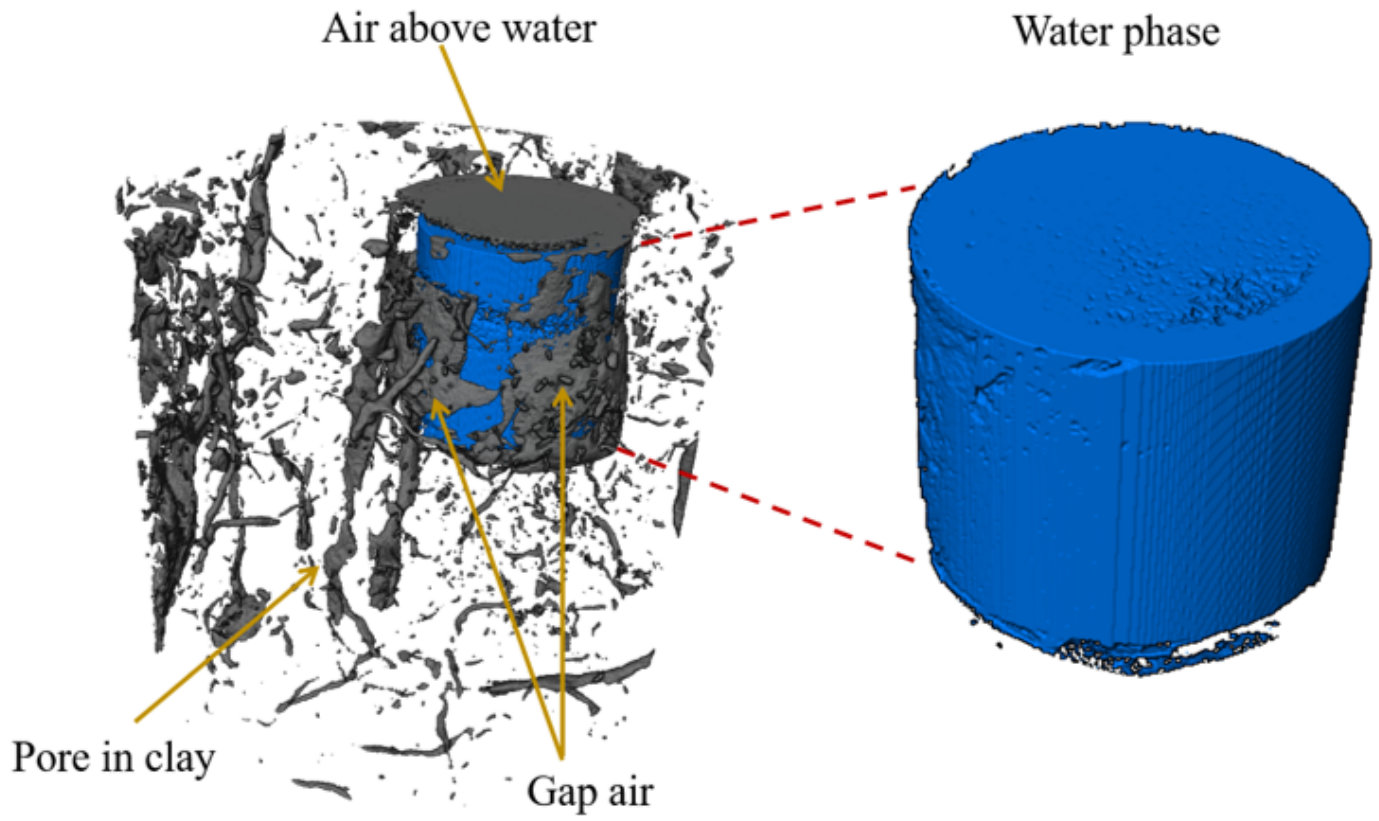
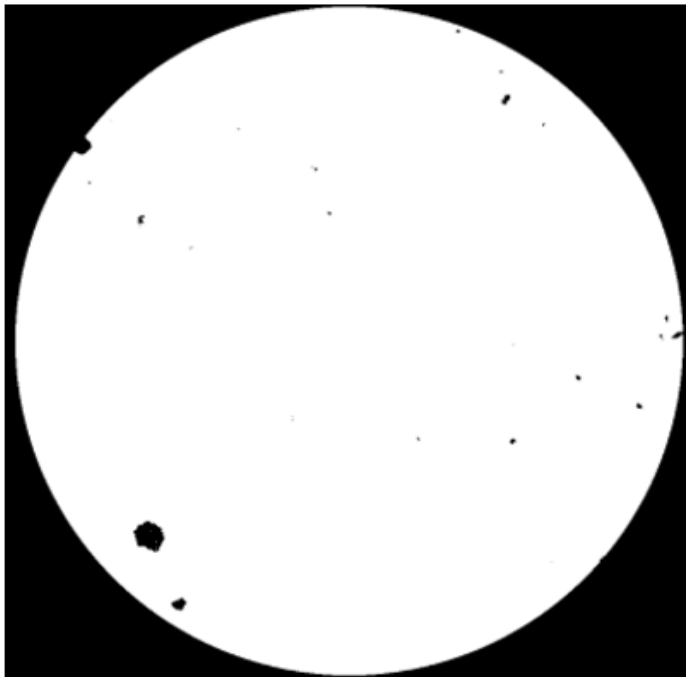
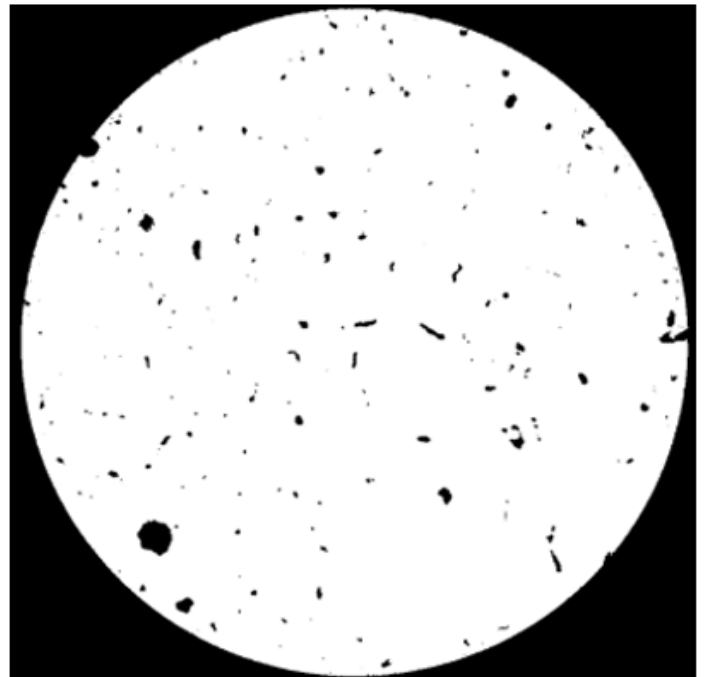


Figure 12

Three-dimensional structure of air and water in the sample



(a)



(b)

Figure 13

Automated thresholding in ImageJ. (a) Otsu (b) Moments

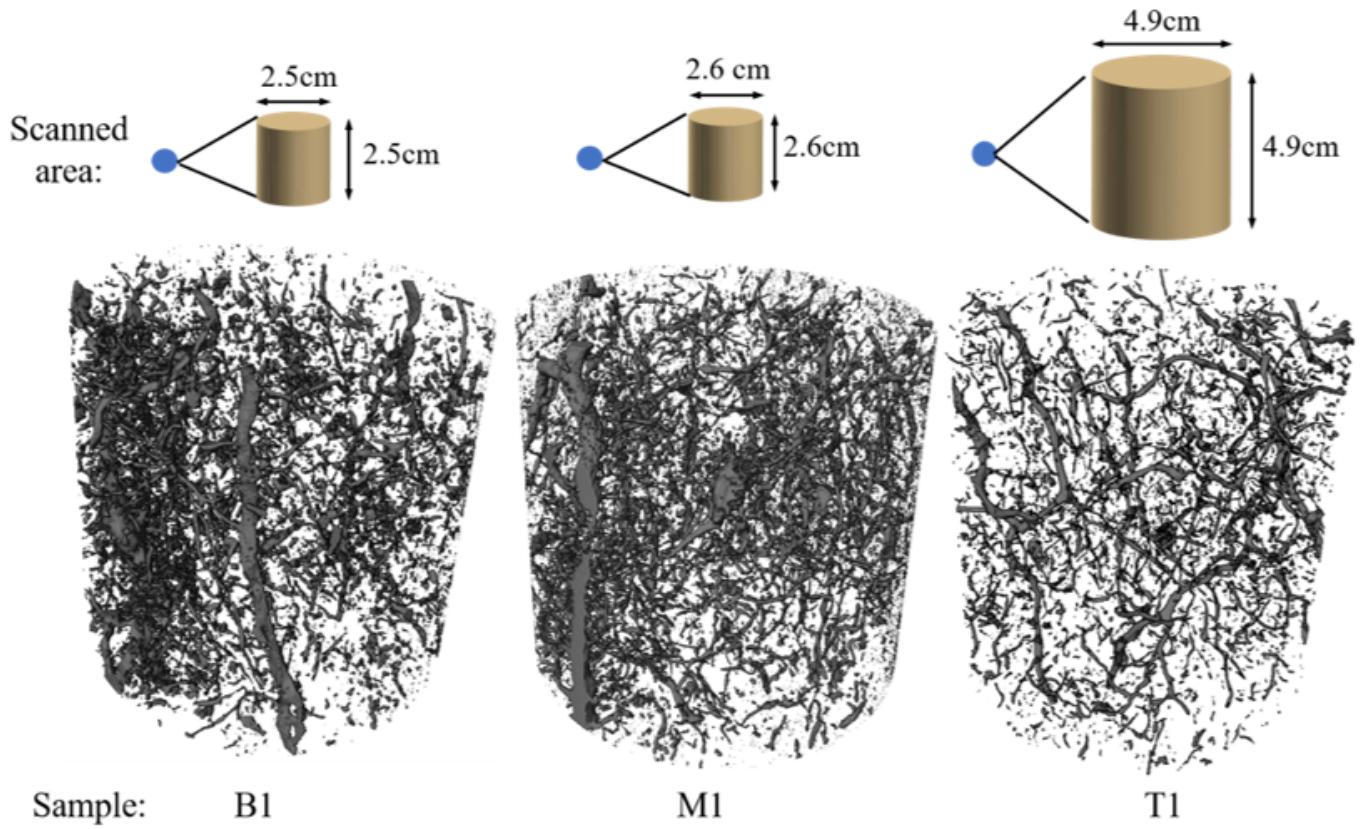


Figure 14

Pore structure of intact Jinan red clay sample

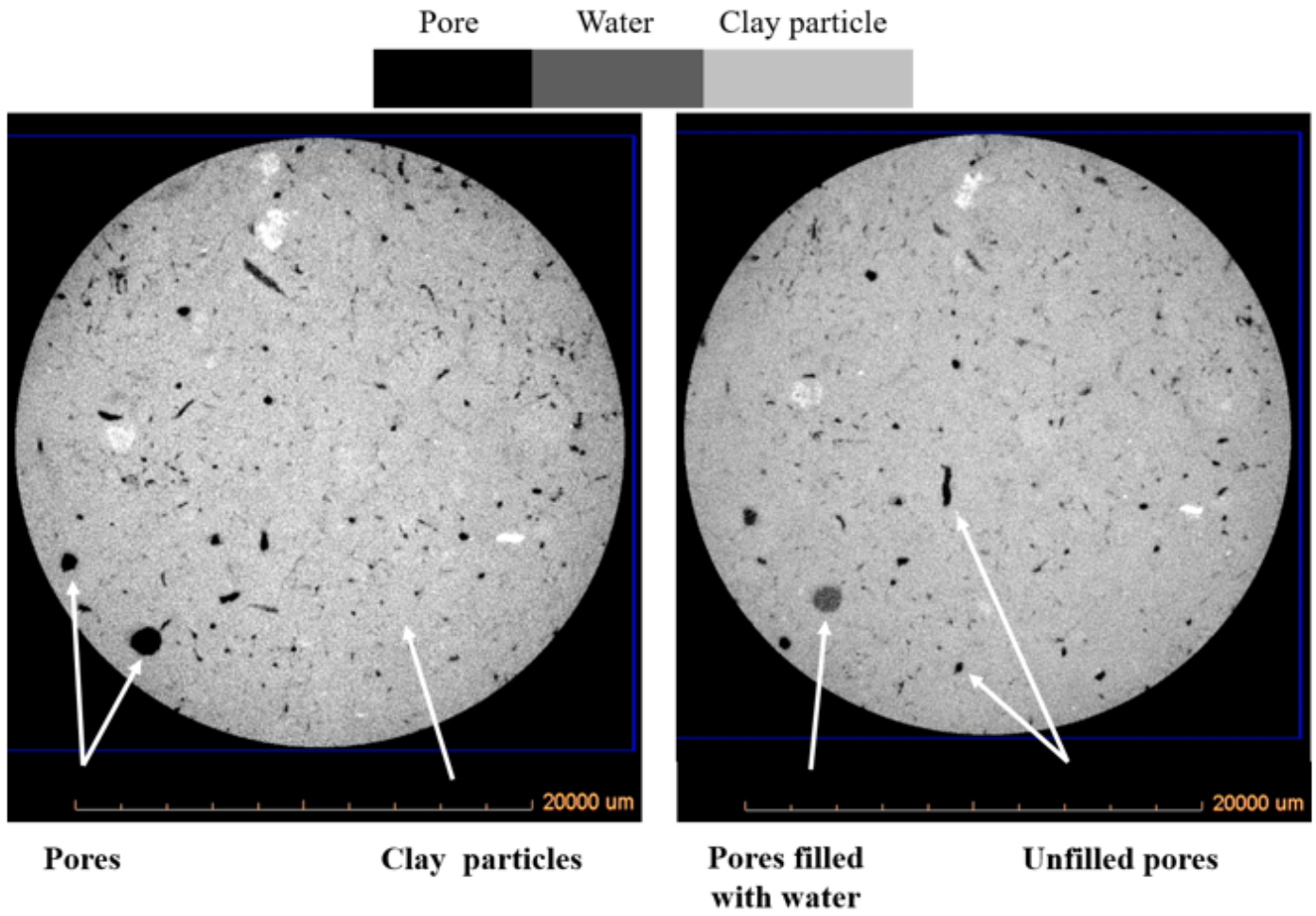


Figure 15

Typical horizontal cross sections of the Jinan red clay sample: (a) Before seepage experiment, and (b) Intermediate stage of seepage experiment

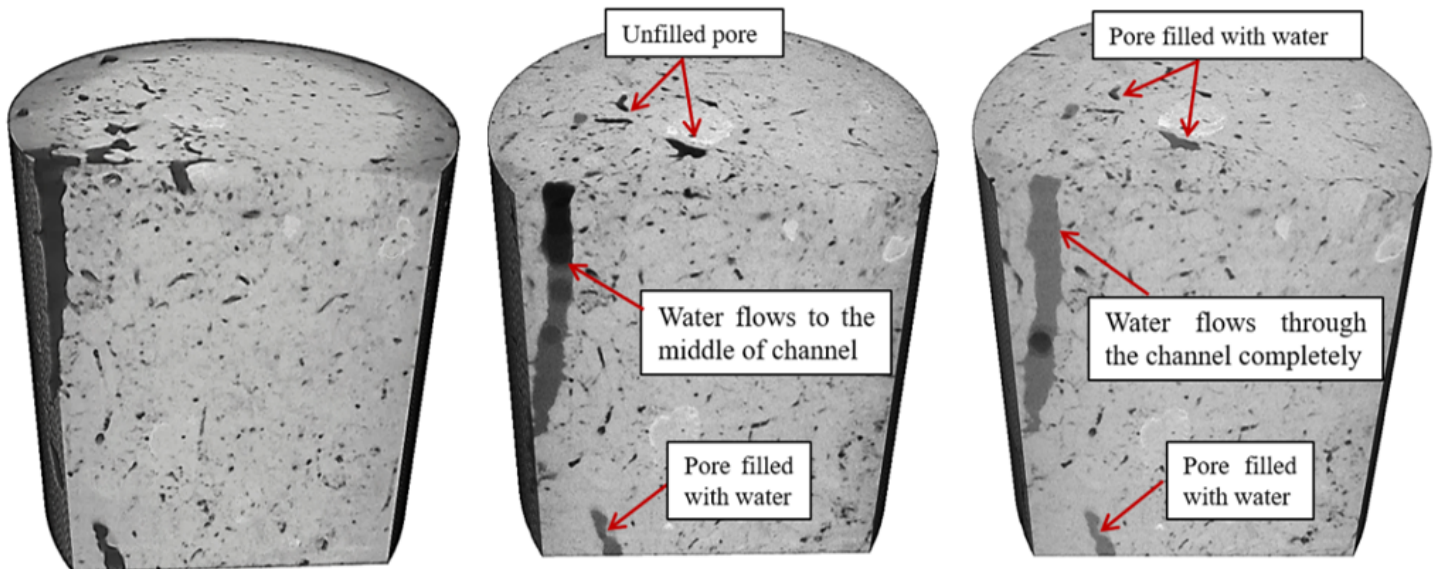


Figure 16

Vertical slices in the YZ plane of 3D reconstruction of the sample under different seepage stages: (a) intact sample; and (b) Intermediate stage of seepage experiment; and (c) End stage of seepage experiment

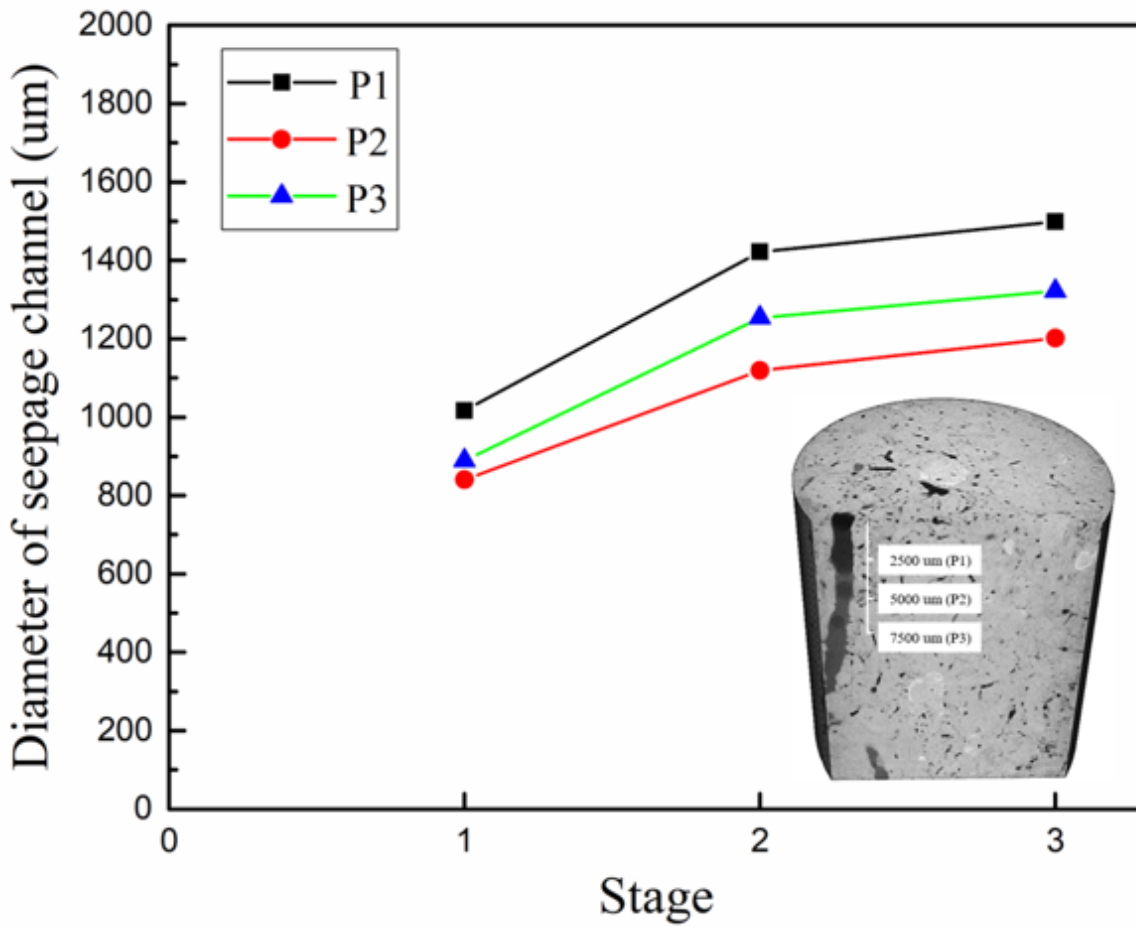


Figure 17

Diameter variation of seepage channel at different positions under three stages

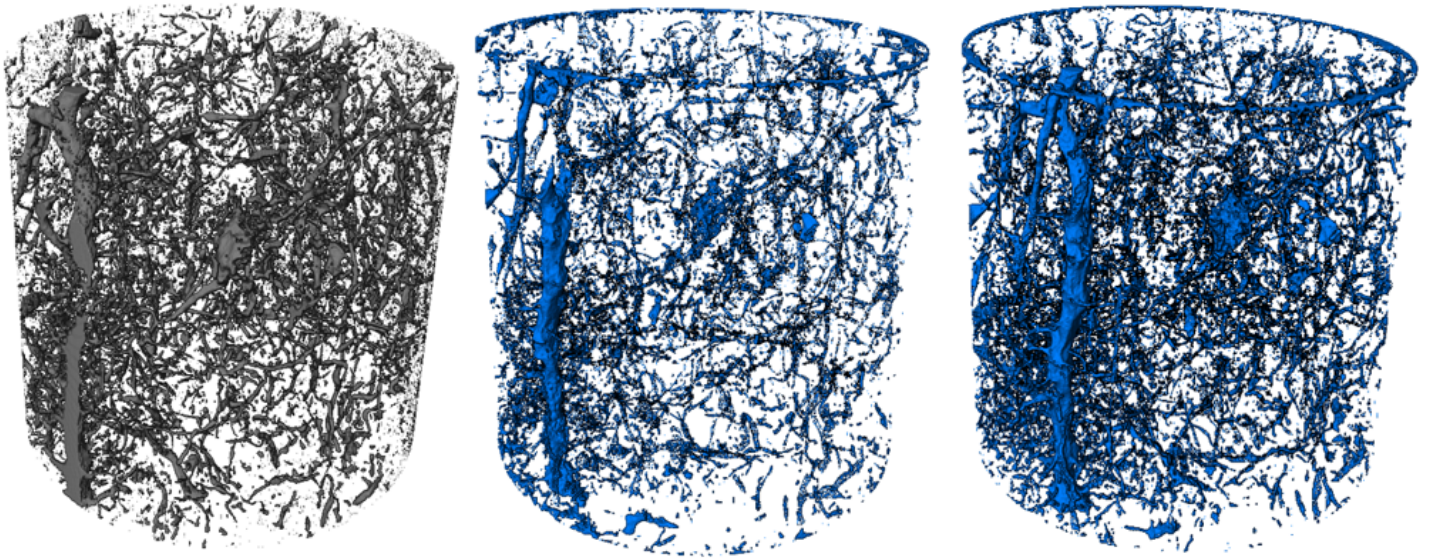


Figure 18

Three-dimensional structure of air and water in sample at different stages based on watershed segmentation algorithm: (a) Intact sample (Pore space), and (b) Intermediate stage of seepage experiment (Water), and (c) End stage of seepage experiment (Water)

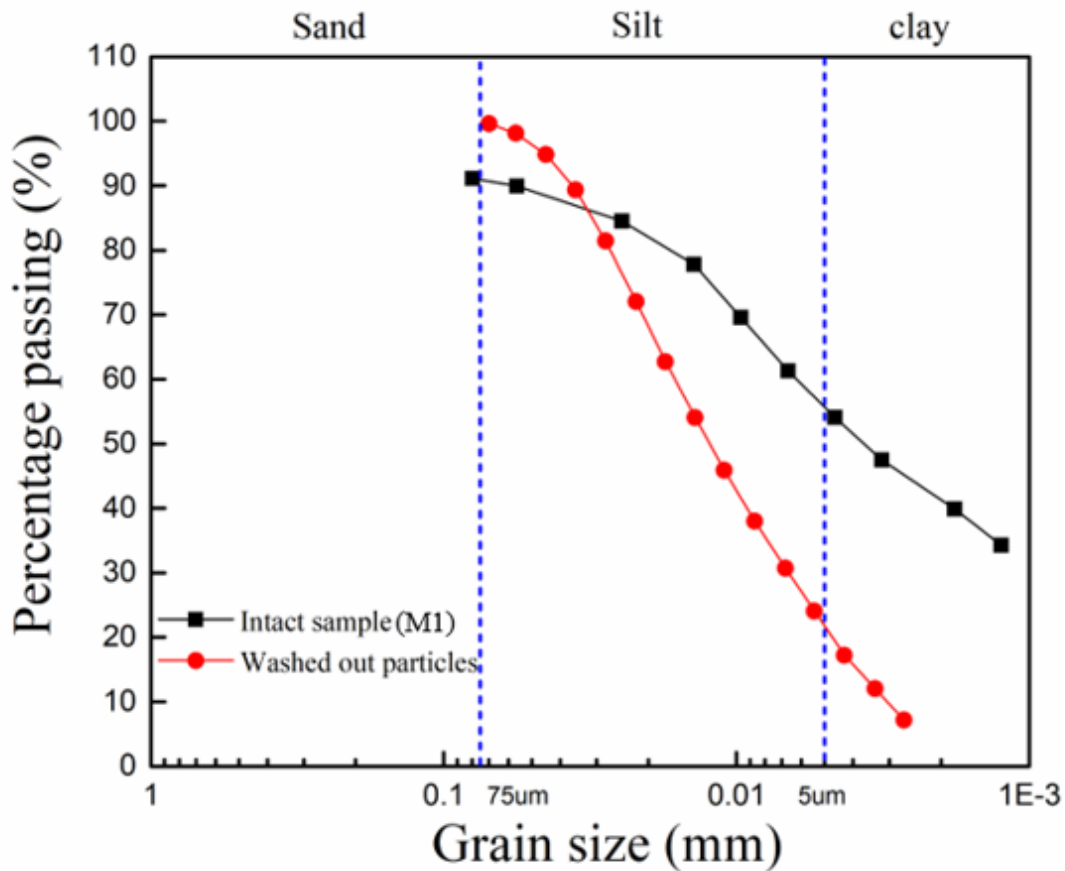


Figure 19

Comparison of grain size distribution of intact Jinan red clay and washed out particles

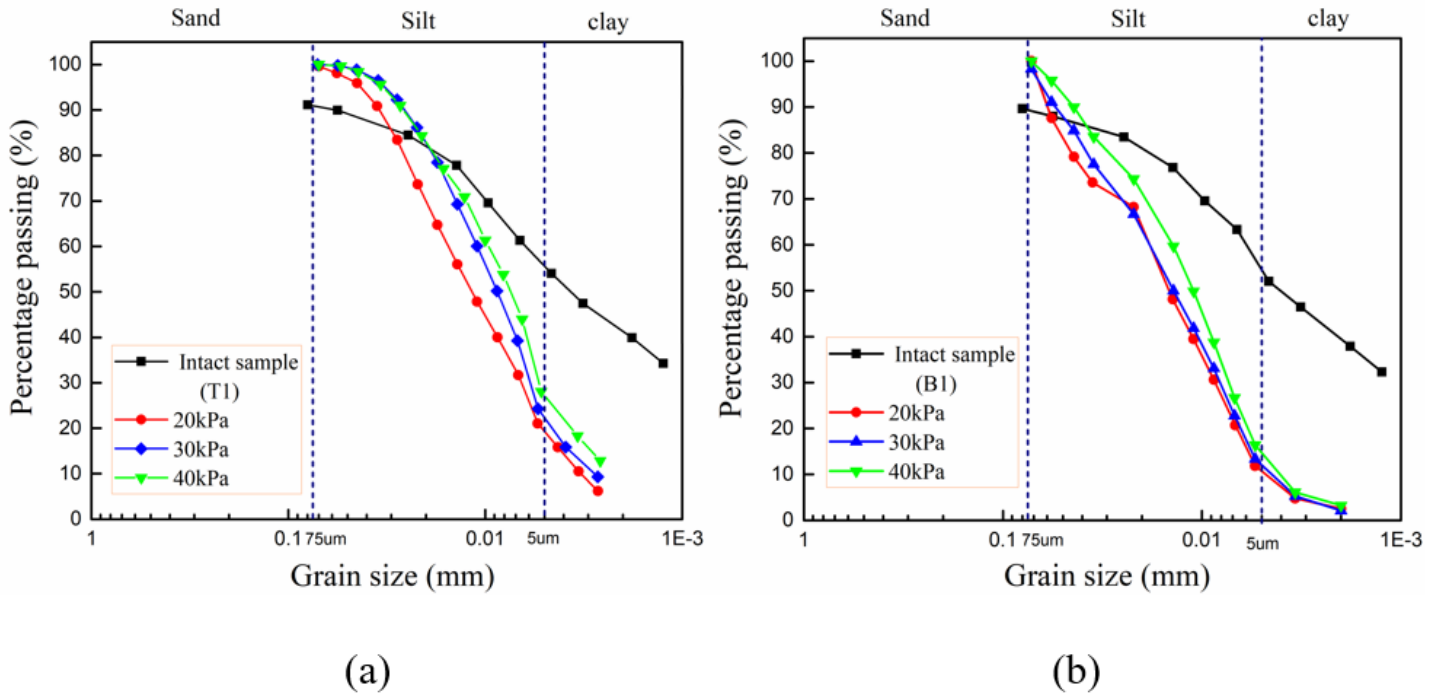


Figure 20

Comparison of grain size distribution of intact Jinan red clay and washed out particles under different water supply pressures (a) T1 sample, and (b) B1 sample

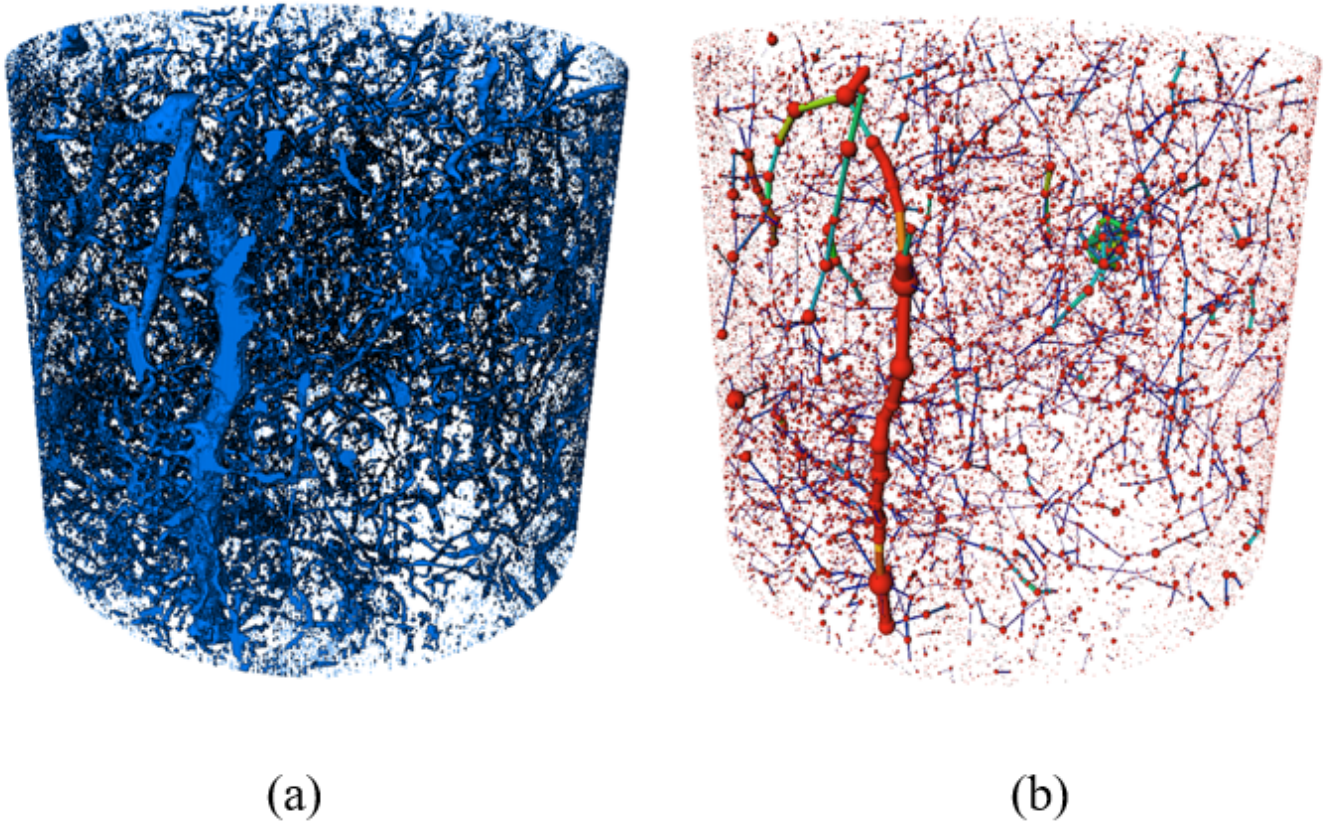


Figure 21

Three-dimensional structure of pore space: (a) Raw pore space structure, and (b) Pore network model (PNM)

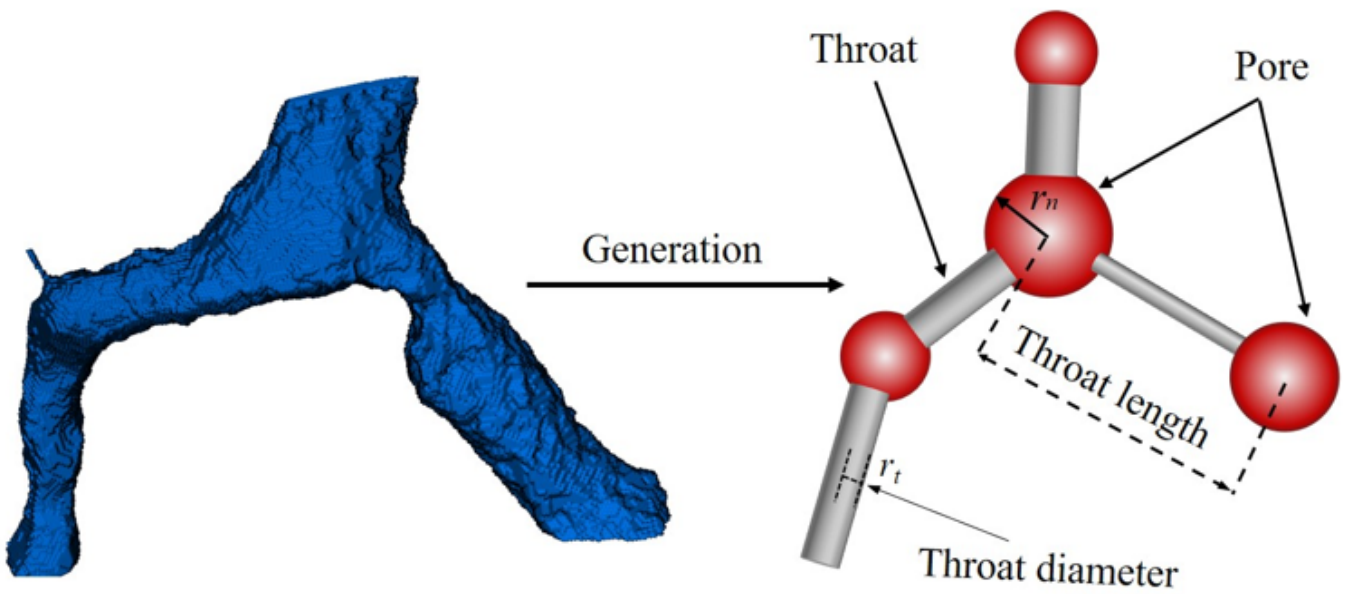


Figure 22

Schematic diagram to generate PNM

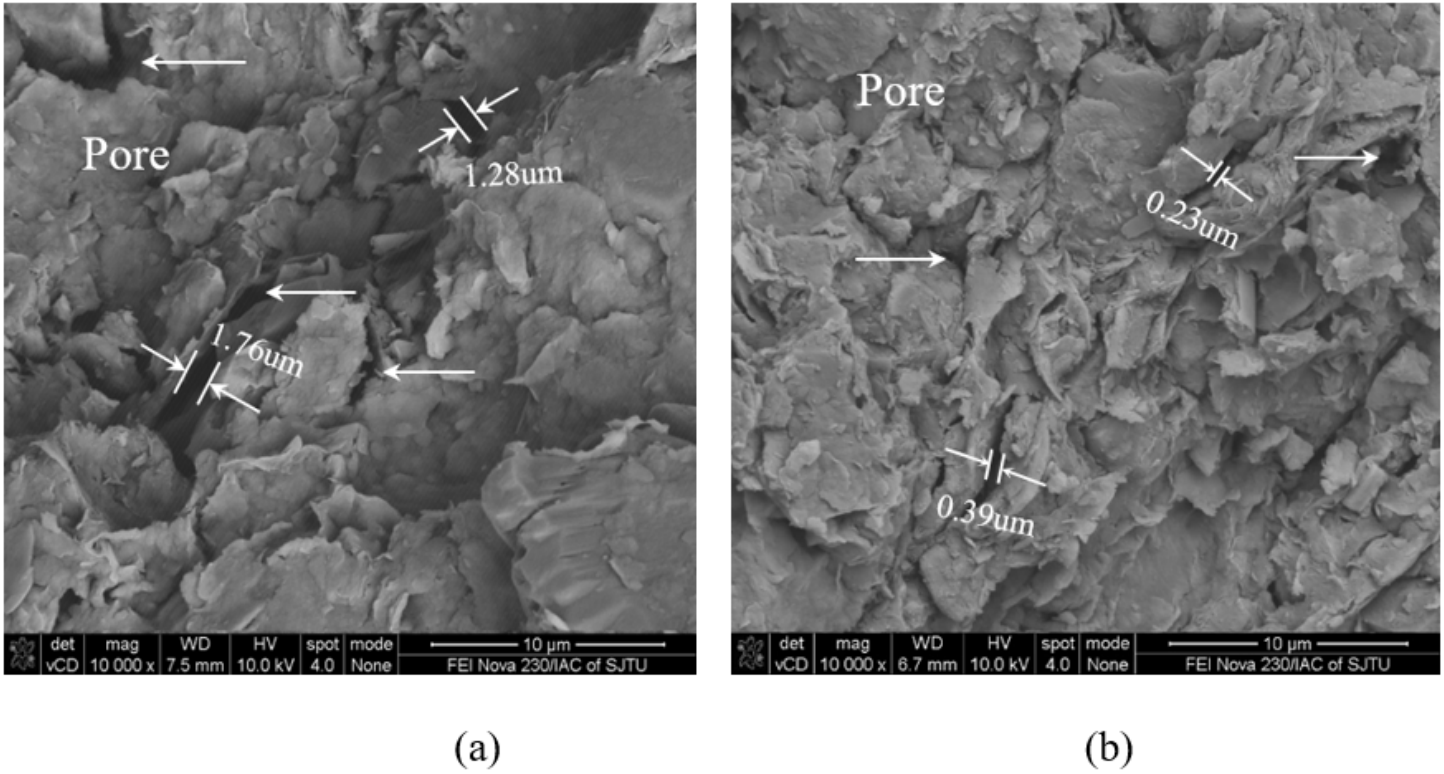


Figure 23

SEM image of Jinan red clay: (a) Horizontal section, and (b) Vertical section

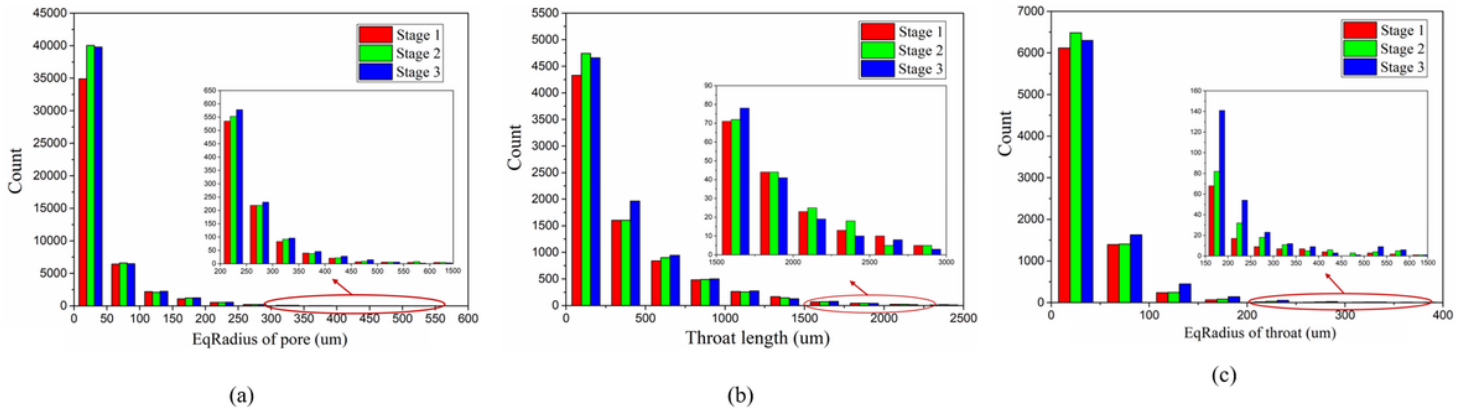


Figure 24

Pore and throat size distributions of Jinan red clay under three different stages of the whole experiment: (a) Pore diameter distribution (b) Throat length distribution (c) Throat diameter distribution

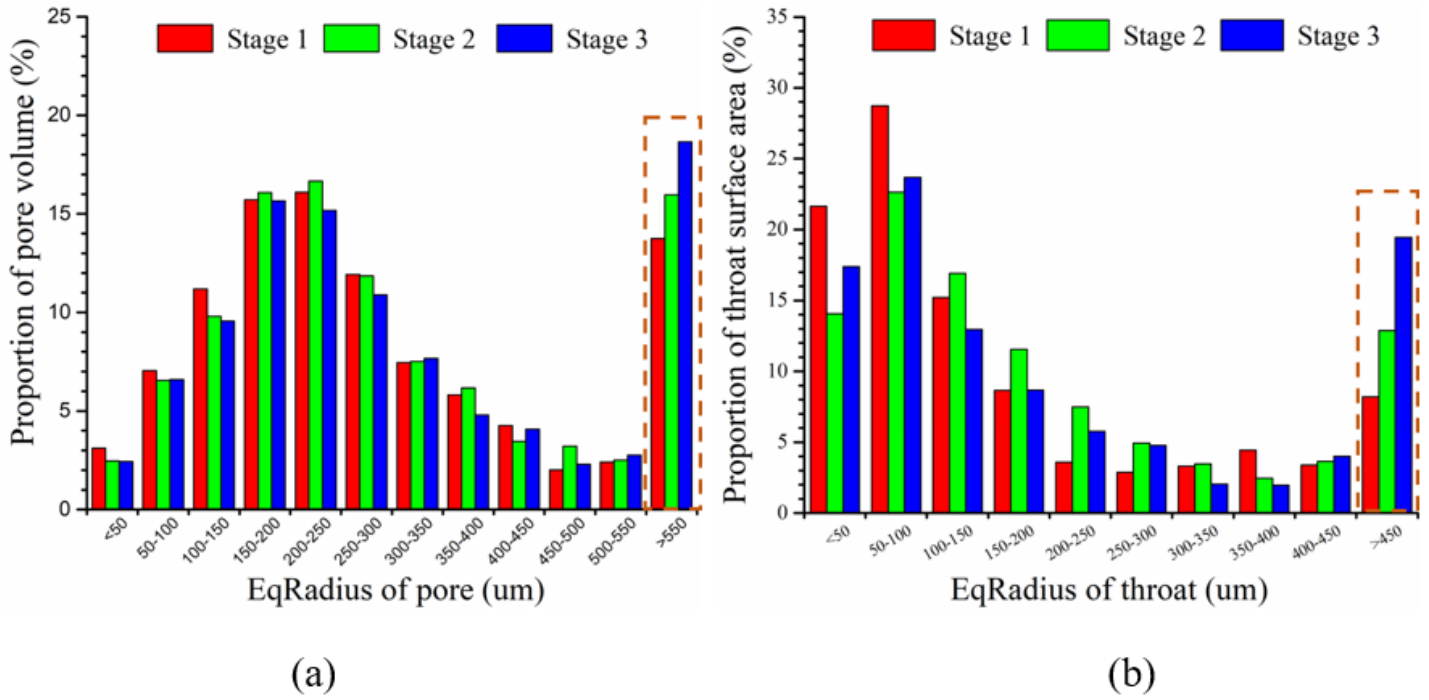


Figure 25

Distribution of pore volume proportion and throat surface area proportion of Jinan red clay under three different stages of the whole experiment (a) pore volume proportion (b) throat surface area proportion

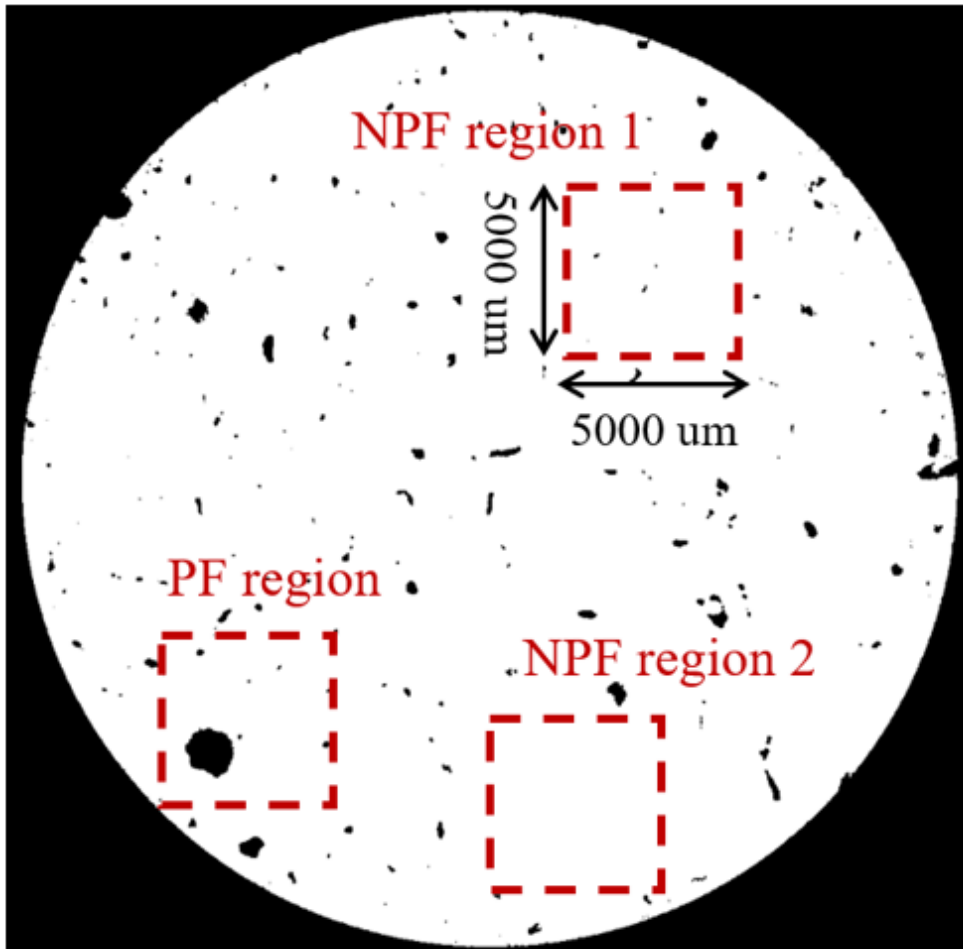


Figure 26

Different ROI regions in horizontal cross sections of sample

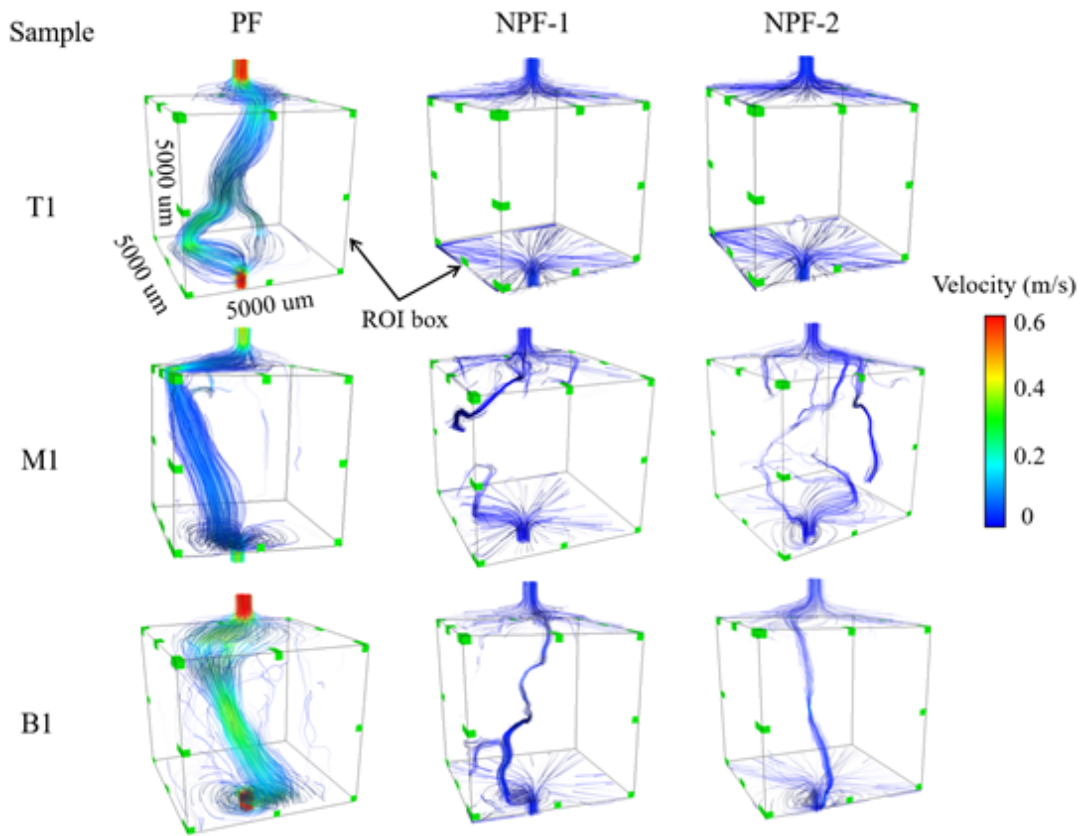


Figure 27

Seepage simulation results of streamlines for different ROI of samples

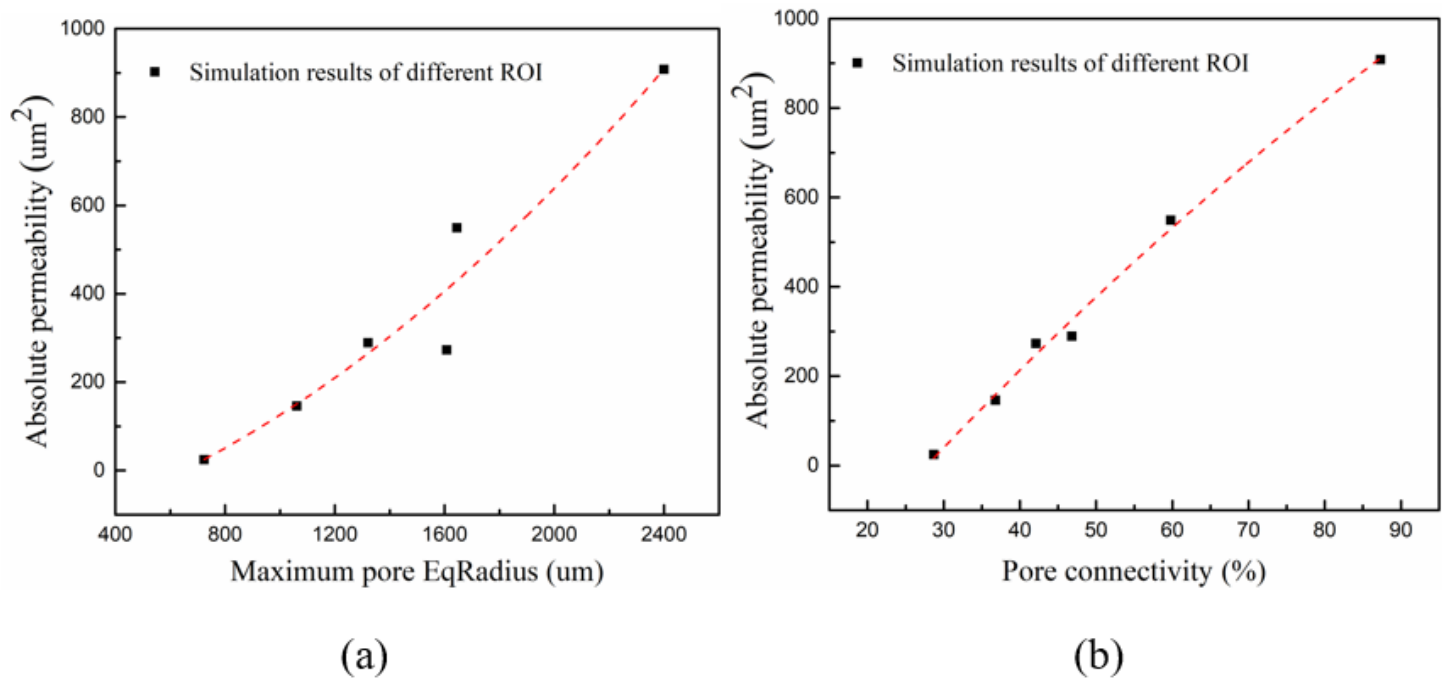


Figure 28

The relation curve between absolute permeability and pore parameters: (a) maximum pore EqRadius, and (b) pore connectivity